Optimal Design of a Guided Wave Rail Web Transducer using Numerical Modeling

Dineo A. Ramatlo

UNIVERSITEIT VAN PRETORIA
UNIVERSITY OF PRETORIA
YUNIBESITHI YA PRETORIA

Optimal Design of a Guided Wave Rail Web Transducer using Numerical Modeling

by

Dineo A. Ramatlo

Submitted in partial fulfillment
of the requirements for the degree

Master of Engineering (Mechanical)

in the

Department of Mechanical and Aeronautical Engineering
Faculty of Engineering, the Built Environment and Information Technology

University of Pretoria
Pretoria
South Africa

May 2016

Abstract

Title: Optimal Design of a Guided Wave Rail Web Transducer using Numerical Modelling

Student name: D.A. Ramatlo

Supervisor: Dr. D.N. Wilke (supervisor)

Dr. P.W Loveday (co-supervisor)

Dr. C.S Long (co-supervisor)

Department: Mechanical and Aeronautical Engineering

Degree: MEng (Mechanical)

Date: 2016

Ultrasonic Guided Waves can propagate over long distances, and are thus suitable for the interrogation of long structural members such as rails. A recently developed Ultrasonic Broken Rail Detection (UBRD) system for monitoring continuously welded train rail tracks, primarily detects complete breaks. This system uses a guided wave mode with energy concentrated in the head of the rail, which propagates large distances and which is suitable for detecting defects in the rail head. Exploiting a second mode, with energy concentrated in the web section, would allow us to effectively detect defects in the web of the rail.

The objective of this study is to develop an ultrasonic piezoelectric transducer that can excite a guided wave mode with energy concentrated in the web of the rail. It is required

that the transducer must strongly excite such a mode at the operational frequency of the UBRD system. The objective is thus to obtain a design with optimal performance.

A recently developed numerical modelling technique is used to model the interaction of the transducer with the rail structure. The technique employs a 2D Semi-Analytical Finite Element (SAFE) mesh of the rail cross-section and a 3D finite element mesh of the transducer; and is thus referred to as SAFE-3D. The accuracy of the SAFE-3D method was validated though experimental measurements performed on a previously developed transducer.

A design objective function representative of the energy transmitted by the transducer to the web mode was selected. The identified design variables were the dimensions of the transducer components. The performance of the transducer was optimized using a response surface-based optimization approach with a Latin Hypercube sampled design of experiments (DoE) that required SAFE-3D analyses at the sampled points. A Nelder-Mead optimization algorithm was then used to find an optimal transducer design on the response surface.

The performance of the optimal transducer predicted by the response surface was found to be in good agreement with that computed from SAFE-3D. The optimum transducer was manufactured and experimental measurements verified that the transducer model was exceptionally good. The design method adopted in this study could be used to automate the design of transducers for other sections of the rail or other frequencies of operation.

KEYWORDS: Ultrasonic guided wave; Piezoelectric transducer; SAFE-3D; Optimization

Publications

The following publications were produced as part of this study:

1. D. A. Ramatlo., C. S. Long., P. W. Loveday and D. N. Wilke.; "SAFE-3D analysis of a piezoelectric transducer to excite guided waves in a rail web", *in Review of Progress in Quantitative Nondestructive Evaluation*, eds. D. E. Chimenti and L. J. Bond, (American Institute of Physics 1706, Melville, NY) 020005 (2016).

2. D. A. Ramatlo., D. N. Wilke and P. W. Loveday.; "Optimal Design of a Piezoelectric Transducer for Exciting Guided Wave Ultrasound in Rails", *43rd Annual Review of Progress in Quantitative Nondestructive Evaluation*, Georgia, 16-22 July 2016.

3. D. A. Ramatlo., D. N. Wilke and P. W. Loveday.; "Optimal Design of a Piezoelectric Transducer to Excite Ultrasonic Guided Waves", *10th South African Conference on Computational and Applied Mechanics*, South Africa, 3-5 October 2016.

4. D. A. Ramatlo., D. N. Wilke and P. W. Loveday.; "Development of an Optimal Piezoelectric Transducer to Excite Guided Waves in a Rail Web", *Submitted to NDT & E International Journal*, 2016.

Acknowledgements

I would like to acknowledge the following people for their help and support:

- Dr. Craig Long, for introducing me to the field of guided wave modelling and greatly contributing to the early development of this study. The 'SAFE-3D' code used for modelling the transducer attached to the rail was developed by Dr. Long.
- Dr. Philip Loveday and Dr. Nico Wilke, for their guidance during this study. I am very grateful for all their input and feedback. Without their valuable contribution, including that of Dr. Long, this study would never have been a success.
- Mr. Andre Grobler and Mr. Petrus Kabini, for helping with the manufacturing of the transducer components.
- Mr. Irvine Marrian and Mrs. Gail Marrian, for helping with the assembling of the transducer system.
- Mr. David Seshai, for helping to conduct lab tests on the manufactured transducer.

Special thanks due to :

- The CSIR for granting me this wonderful opportunity to further my studies.
- Ms. Evonne Thathane and Mr. Stanley Hlatswayo from Trac SA, my aunt Mrs. Mmathapelo Mdlalose and my uncle Mr. Llifi Ramatlo. Thank you for giving me the key to my dreams.

Personal thanks due to :

- My mother Ms. Deborah Ramatlo and my grandmother Ms. Ephenia Ramatlo, to whom I dedicate this thesis. Mom, thank you for being the best. It is all the qualities you possess that shaped me to grow into the woman I am today. *Koko*, I will never forget all the huge sacrifices that you and the entire Ramatlo clan always made to help *mama* with bringing me up. For that, I deeply thank *SEDIBANE'A NKOKOTLELA*.
- My father Mr. Lucas Ndhlovu. Dad, through you and mom, God gave me a wonderful life that I value with all my heart. "I am because of you".

Finally, I would like to thank God for all the strength and wisdom that He always provides me with.

Contents

List of Figures

List of Tables

Nomenclature

c	Elasticity	N/m^2
d	Charge density constant	C/N
D	Dielectric displacement / Dynamic stiffness	C/m^2 or N/m
e	Permittivity of material	F/m
E	Young's Modulus / Electric field	N/m^2 or V/m
E_k	Kinetic energy	J
f	Force / Frequency	N or Hz
F	Force	N
g	Voltage constant	Vm/N
K	Relative dielectric constant	-
$\mathbf{K}$	Stiffness matrix	N/m
$\mathbf{M}$	Mass matrix	kg
N	Sample size / Shape functions / Number of DoFs	-
$N_{,x}$, $N_{,y}$, $N_{,z}$	Shape function derivatives	-
q	Electrical charge	C
R	Receptance	m/N
S	Piezoelectric strain	mm/mm
t	Time	s
T	Piezoelectric stress	N/m^2
u, v, w	Displacement fields	m
$\dot{u}$	Velocity	m/s
U	Displacement	m
v_g, v_p	Group / Phase velocity	m/s
V	Volume	m^3
x, y, z	Local axis system, also denotes sample set	m or -
x_1, x_2, x_3	Design variables	-

Greek letters

α	Modal amplitude	-
ϵ	Permittivity	F/m
ε	Strain	mm/mm
ε_0	Permittivity of free space	F/m
κ	Wave number	rad/m
ν	Poison's ratio	-
ρ	Density	kg/m^3
σ	Stress	N/m^2
ϕ	Electrical potential	V
ψ	Mode shape	-
ω	Natural frequency	rad/s

Abbreviations

BM	Back Mass
CSIR	Council for Scientific and Industrial Research
DoE	Design of Experiments
DoF	Degree of freedom
FEM	Finite Element Method
FM	Front mass
IMT	Institute of Maritime Technology
LB	Lower Bound
LHS	Latin Hypercube Sampling
LOOCV	Leave-one-out Cross Validation
PZT	Lead Zicornate Titanate
RBF	Radial Basis Function
SAFE	Semi-Analytical Finite Element
SAFE-3D	Semi-Analytical Finite Element - 3 Dimensional Finite Element
UB	Upper Bound
UBRD	Ultrasonic Broken Rail Detection

CHAPTER 1

Introduction

1.1 Background

Rail Infrastructure in the world is ageing, giving rise to increased development and growth of imperfections like cracks and flaws, which can result in broken rails and ultimately train derailments. To prevent train derailments, there is thus a crucial need for effective rail monitoring systems. Such systems will allow for the continual inspection of the rail, and ultimately help to keep track of defect development and growth, so that action can be taken before the critical stage is reached.

Recently, the Council for Scientific and Industrial Research (CSIR) together with the Institute for Maritime Technology (IMT) have developed an Ultrasonic Broken Rail Detection (UBRD) system for the inspection of rail tracks [6]. The system, currently installed in the Sishen-Saldanha Ore line, uses ultrasonic guided waves transmitted between transmit and receive transducers. If the transmitted signals are not detected by the receive station, an alarm is triggered indicating a broken rail. The UBRD system primarily detects complete rail breaks by using a propagating guided wave mode with energy concentrated in the head of the rail.

Currently, there are plans to upgrade the system to include defect detection and location before the occurrence of a complete break. To successfully implement the concept, a thorough understanding of how the various propagating modes interact with welds and different types of damage is required. A numerical study by Long and Loveday [19] has been conducted to investigate the types of damage that can be detected by using different propagating modes. Four candidate modes suitable for long range propagation were considered in their study. Long and Loveday found out that a symmetric mode with

energy concentrated in the head of the rail (shown in Figure 1.1, and denoted the 'head mode') can be employed to distinguish between various cracks in the head of the rail and thermite welds; whereas a mode with energy concentrated in the web of the rail (shown in Figure 1.1, and denoted 'the web mode' in this study) is suitable for detecting welds and damage in the web of the rail. A piezoelectric ultrasonic transducer that effectively excites the head mode was developed and investigations were conducted experimentally on a new rail track by using a pulse-echo transducer array set-up [22]. The transducer array was found to allow for long range propagation of the head mode and was thus working effectively. A thermite weld was detected at a distance of $790m$ from the array [22], on a new rail track.

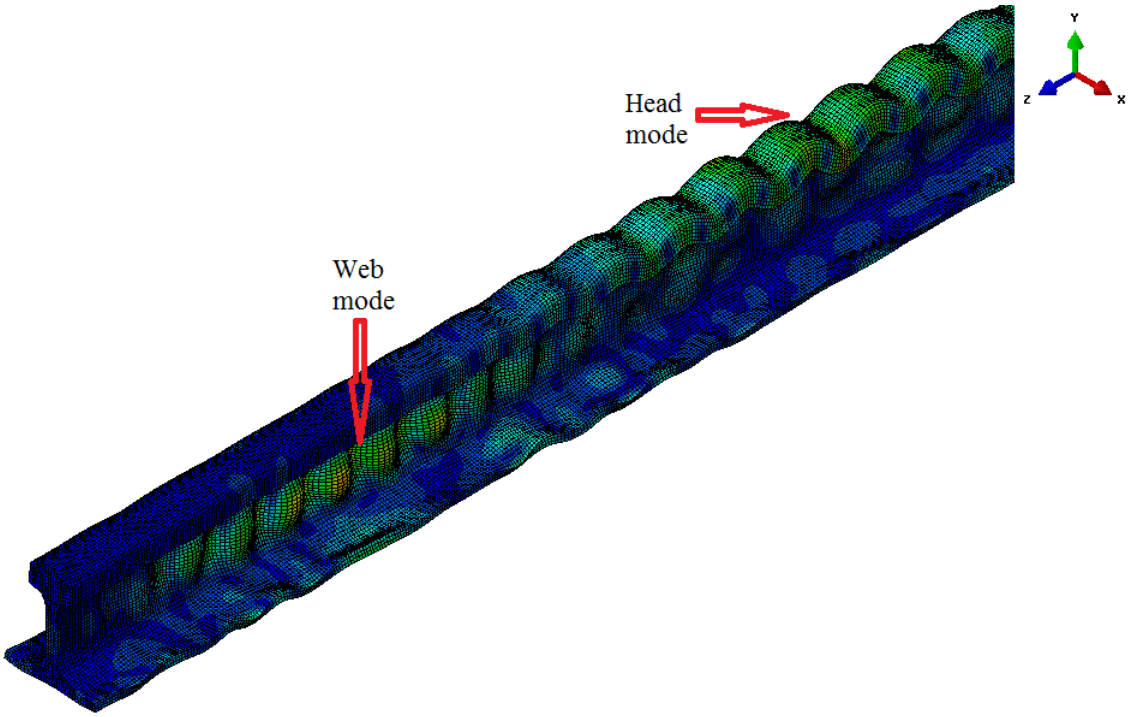

Figure 1.1: The propagation of the head and web modes in a rail track.

Since a transducer suitable for exciting the head mode has been developed, there is now a requirement to develop a transducer to effectively excite the web mode.

The study of guided waves is complicated as there are many different modes of propagation in a wave guide. A thorough understanding of how multiple modes propagate independently, and interact with defects and geometrical features is therefore essential. An introduction to the theory and application of guided waves is presented in the textbook of Rose [29]. Theoretical models of simple wave guides like rods, beams and plates has been explained, but no attention has been given to complex wave guides such as

rail tracks. Theoretical modelling has some limitations and may thus fail to predict all aspects of the solution, especially when the analysis geometry gets complex. To avoid such limitations, it is therefore necessary to follow a numerical modelling approach.

To date, various numerical modelling techniques for guided waves have been presented in the literature. Examples of such techniques includes the finite element method, the finite difference method, the boundary element method and the Semi-Analytical Finite Element (SAFE) method [8, 12, 13, 32]. Many of the numerical modelling techniques are inefficient due to their computational demand. For example, to model wave propagation using the traditional finite element method, a complete three-dimensional geometry of the waveguide structure has to be modelled for a significant portion of the length of the waveguide. The required cost of computation is thus very high, and increases proportionally with the size or length of the waveguide and the frequency of operation. Moreover, the complexity of the problem increases as care has to be taken for the wave reflections from the boundaries of the wave guide. One way to do this is to include absorbing boundary conditions at the ends of the model. However, the computational inefficiencies still remain. These computational inefficiencies are amplified when multiple analyses are to be conducted as is required during the optimal design of transducers. The SAFE method has recently become widely adopted for studying wave propagation due to its reliability [9, 23] and efficiency [1]. In the SAFE method, only a 2D cross-sectional mesh of a waveguide is employed, while the length terms are treated analytically. The method is therefore attractive due to its improved computational efficiency in particular when optimal transducer design is considered, as we will explore in this study.

Numerous work on ultrasonic guided waves in rail structures using the SAFE method has been presented by a number of authors. Gavric [12] and Hayashi [14] studied the dispersion characteristics of a rail waveguide while work on the vibration of a supported rail was conducted by Li et al. [18]. A method for modelling the excitation of guided waves by a piezoelectric transducer was proposed by Loveday [20, 21]. The method employs a 3D traditional finite element mesh of the transducer and attaches it to a 2D SAFE mesh of the waveguide through coincident finite element nodes. An improved version of the method, (referred to as SAFE-3D in this study) which allows for the attachment of the transducer to the waveguide model through non-coincident nodes was later proposed by Loveday and colleagues at the CSIR. In this study, the advantages of using the SAFE-3D method are explained. The method is thus employed to design a piezoelectric transducer to strongly excite the web mode. The transducers used in the UBRD system are resonant transducers designed to transfer significant energy to the rail to achieve long range operation. It is therefore important to correctly capture the dynamics of the transducer in the analysis. The SAFE-3D method allows for this.

To ensure that the maximum energy is transferred into the web mode, the transducer design needs to be optimized. A formal design optimization procedure is outlined by Arora [2]. In design optimization, an objective function quantifying the performance of a design as a function of input variables is required. For the design problem in this paper, the objective function is known, however it is not practical to compute directly as it is implicit. Taking note that multiple analyses will be required, the computation of objective function and sensitivities will be very expensive. Furthermore, difficulty may be experienced when dealing with noisy numerical functions. The use of gradient-based optimization methods is therefore not feasible and appropriate methods need to be employed to successfully model the objective. By employing the response surface based method, a meta-model of the objective function can be constructed through a Latin Hypercube Design of Experiments (DoE), which requires SAFE-3D analyses at the sampled points. The capability of using SAFE-3D in DoE with many sampling points makes the SAFE-3D method highly attractive due to its computational efficiency.

1.2 Motivation

The UBRD system primarily detects complete breaks by using the head mode. For the system to prevent rail breaks, cracks need to be detected (before the occurrence of complete breaks) and distinguished from reflections from other discontinuities like welds in the rail. Previous studies have demonstrated that the head mode can help to detect weld reflections at long distances. Based on numerical work, it is believed that exploiting the web mode would allow us to effectively detect defects in the web of the rail and could also help to distinguish between reflections from welds and cracks.

1.3 Problem Statement

It is required to design a piezoelectric transducer that can strongly excite the rail web mode at the operational frequency of the UBRD system.

1.4 Objectives

The main objectives of this study are:

- To determine the strengths and weaknesses of the selected numerical modelling approach in predicting the response of waveguides to excitation. The response to an applied point load and to the excitation by piezoelectric transducers will be studied.

- To use the SAFE-3D numerical modelling method and optimization techniques to design a piezoelectric transducer to excite a mode with energy concentrated in the web of the rail.
- To manufacture the transducer and experimentally validate the modelling approach.

1.5 Scope of Work

To complete this study, the following tasks were carried out:

- The SAFE method was implemented in MATLAB. The code was used to study a forced response problem where guided waves in the rail were excited by a point load.
- The forced response problem was also modelled in ABAQUS, for comparison to the SAFE results and to verify the correct implementation of the method.
- The SAFE-3D method which had already been implemented in MATLAB by the CSIR was adopted to model the excitation of guided waves using a transducer, and the results obtained were validated by experimental measurements.
- A response surface-based optimization process that employed a Latin hypercube sampled design of experiments was implemented in MATLAB. A total of 500 SAFE-3D analyses in the design space were required to develop the response surface. Gradient based optimization on the response surface was used to find the optimal transducer design.
- The optimum transducer design for the web mode was manufactured, and experimental measurement was performed to validate the design.

1.6 Overview of Dissertation

Chapter 2: Guided wave modelling using the SAFE method

A brief introduction to the SAFE method is presented, followed by a thorough explanation of the formulation of the method. Thereafter, the SAFE method is adopted to study the free vibration characteristics of a rail and the rail web mode forced response problem, which is also studied using ABAQUS to verify the SAFE results. The chapter also presents the limitations of the SAFE method and possible strategies to help counteract such limitations.

Chapter 3: Modelling of a Piezoelectric Transducer Attached to a Wave Guide Using the SAFE-3D Method

The modelling of a piezoelectric transducer using the traditional finite element method is first presented. By employing the 3D finite element transducer model and the 2D SAFE model of the rail from Chapter 2, the SAFE-3D method is then thoroughly explained. Finally, the method is applied to predict the excitation of the web mode using an available transducer, and experimental measurements are used to validate the SAFE-3D results. This chapter is based on the work presented at the *42nd Annual Review of Progress in Quantitative Nondestructive Evaluation.*

Chapter 4: Design Optimization of a Piezoelectric Transducer to Excite Guided Waves in a Rail Web

A brief introduction to design optimization is first presented. A formal optimization formulation for the design of a rail web transducer is then presented in detail. Thereafter, a response surface method with a Latin Hypercube sampled DoE (that required SAFE3D analyses at the sampled points) is employed to construct a meta-model of the objective function of the transducer design. A Nelder-Mead optimization algorithm is then used to find an optimal transducer design on the response surface. This chapter is based on the work to be presented at the *10th South African Conference on Computational and Applied Mechanics*, which will be published in the conference proceedings.

Chapter 5: Manufacturing and Validation of the Optimal transducer design

The optimal transducer design from Chapter 4 was manufactured. Experimental measurements were performed on a rail segment to validate the predicted performance of the optimal transducer design.

Chapter 6: Conclusions and Recommendations

The conclusions and recommendation are presented in Chapter 6. The suggestions for future work are also stated.

CHAPTER 2

Guided Wave Modelling using the Semi-Analytical Finite Element Method

Modelling the propagation of stress waves in long structural members can be performed efficiently by using the SAFE method. The method can be used to provide a thorough understanding of the various modes of propagation in a waveguide. In this Chapter, the concept of guided wave modelling using the SAFE method is introduced and implemented to compute the propagation in a rail.

2.1 Introduction

SAFE is a 3D analysis technique that only requires a 2D cross-sectional mesh of the wave guide. The method is based on the assumption that the displacements of a point in a waveguide are functions of position and time. The displacement, strain and stress fields are interpolated over the waveguide cross-section, while the variation along the length is treated analytically. The highly reduced computational cost and the absence of boundary reflections makes the SAFE method very attractive. Displacements at various distances can be computed without additional effort being required. One limitation of the SAFE method is that it requires the cross-section of the waveguide to be constant through out its length, and thus extend with only straight edges.

2.2 SAFE formulation

The SAFE formulation presented in this section follows that of Hayashi [14].

2.2.1 Governing relations

An infinite elastic wave guide with an arbitrary cross-section in the $xy - plane$ is considered, as shown in figure 2.1. The cross-section is constant and thus extends along the $z - direction$ with straight edges.

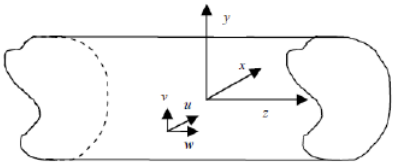

Figure 2.1: Infinite wave guide with arbitrary cross-section, [21].

The displacement, strain and stress vectors for a point on the cross-section of the wave guide are respectively defined as:

$$\mathbf{u} = \{u, v, w\}^T \tag{2.1}$$

$$\varepsilon = \{\varepsilon_{xx}, \varepsilon_{yy}, \varepsilon_{zz}, \gamma_{xy}, \gamma_{yz}, \gamma_{xz}\}^T \tag{2.2}$$

$$\sigma = \{\sigma_{xx}, \sigma_{yy}, \sigma_{zz}, \tau_{xy}, \tau_{yz}, \tau_{xz}\}^T \tag{2.3}$$

For a wave propagating along the $z - direction$, the displacement fields in the x, y and z directions are expressed in complex exponential form [14], respectively as:

$$u(x, y, z, t) = u(x, y)e^{-j(kz-wt)} \tag{2.4}$$

$$v(x, y, z, t) = v(x, y)e^{-j(kz-wt)} \tag{2.5}$$

$$w(x, y, z, t) = w(x, y)e^{-j(kz-wt)} \tag{2.6}$$

where κ is the wave number in rad/m, w is the circular natural frequency in rad/s and the parameter t denotes the time.

From the definition of strain, equation 2.2 is expanded as:

$$\varepsilon = \begin{Bmatrix} \frac{\partial u}{\partial x} \\ \frac{\partial v}{\partial y} \\ \frac{\partial w}{\partial z} \\ \frac{\partial u}{\partial y} + \frac{\partial v}{\partial x} \\ \frac{\partial v}{\partial z} + \frac{\partial w}{\partial y} \\ \frac{\partial u}{\partial z} + \frac{\partial w}{\partial x} \end{Bmatrix} \tag{2.7}$$

After substituting equations 2.4 to 2.6 into 2.7, the strain can be decomposed into terms that are respectively independent and dependent on the wave number κ:

$$\varepsilon = \left[\begin{Bmatrix} \frac{\partial u}{\partial x} \\ \frac{\partial v}{\partial y} \\ 0 \\ \frac{\partial u}{\partial y} + \frac{\partial v}{\partial x} \\ \frac{\partial w}{\partial y} \\ \frac{\partial w}{\partial x} \end{Bmatrix} - jk \begin{Bmatrix} 0 \\ 0 \\ w \\ 0 \\ v \\ u \end{Bmatrix} \right] e^{-j(kz-wt)} \tag{2.8}$$

The stress field on the element is computed from the constitutive relation as:

$$\sigma = c\varepsilon \tag{2.9}$$

where c is the 6×6 elasticity tensor given by:

$$c = \frac{E}{(1+\nu)(1-2\nu)} \begin{bmatrix} 1-\nu & \nu & \nu & 0 & 0 & 0 \\ \nu & 1-\nu & \nu & 0 & 0 & 0 \\ \nu & \nu & 1-\nu & 0 & 0 & 0 \\ 0 & 0 & 0 & \frac{1-2\nu}{2} & 0 & 0 \\ 0 & 0 & 0 & 0 & \frac{1-2\nu}{2} & 0 \\ 0 & 0 & 0 & 0 & 0 & \frac{1-2\nu}{2} \end{bmatrix} \tag{2.10}$$

The property E is the Young's Modulus and ν is the Poison's ratio of the material.

2.2.2 Variational form

Neglecting external and body forces, it can be shown that using Hamilton's principle and assuming a time harmonic dependence, the variational form is given by [32, 31]:

$$\int_V \delta\varepsilon^T \cdot \sigma dV - \omega^2 \int_V \rho\delta\mathbf{u} \cdot \mathbf{u} dV = 0 \tag{2.11}$$

where ρ is the mass density, and $\delta\varepsilon$ and $\delta\mathbf{u}$ are variations of the strain and displacement respectively. Damljanovic and Weaver [9] showed that with the assumptions of equations

2.4 to 2.6, the variation of the displacement is:

$$\delta \mathbf{u}^T = \delta \mathbf{u}(x,y)^T e^{j(kz-\omega t)} \tag{2.12}$$

2.2.3 Finite element interpolation

For each element e on the wave guide cross-section, the displacement at any point is evaluated by interpolating the nodal displacement vector $\{U^e\}$ with the displacement shape function matrix $\mathbf{N}$.

$$\mathbf{u}(x,y,z,t) = \mathbf{N}(x,y)\,\{U^e\}\,e^{-j(\kappa z-\omega t)} \tag{2.13}$$

The interpolation is performed over the cross-section, and the length term is treated analytically.

Following the notation of Hayashi [14], equation 2.8 can also be expressed as:

$$\varepsilon = \left[\mathbf{L}_x\frac{\partial}{\partial x} + \mathbf{L}_y\frac{\partial}{\partial y} + \mathbf{L}_z\frac{\partial}{\partial z}\right]\mathbf{u} \tag{2.14}$$

where

$$\mathbf{L}_x = \begin{bmatrix} 1 & 0 & 0 \\ 0 & 0 & 0 \\ 0 & 1 & 0 \\ 0 & 0 & 0 \\ 0 & 0 & 0 \\ 0 & 0 & 1 \end{bmatrix}, \mathbf{L}_y = \begin{bmatrix} 0 & 0 & 0 \\ 0 & 1 & 0 \\ 0 & 0 & 0 \\ 1 & 0 & 0 \\ 0 & 0 & 1 \\ 0 & 0 & 0 \end{bmatrix} \; and \; \mathbf{L}_z = \begin{bmatrix} 0 & 0 & 0 \\ 0 & 0 & 0 \\ 0 & 0 & 1 \\ 0 & 0 & 0 \\ 0 & 1 & 0 \\ 1 & 0 & 0 \end{bmatrix} \tag{2.15}$$

Now substituting equation 2.13 into the strain-displacement relation in 2.14 leads to:

$$\begin{aligned} \varepsilon &= \left[\mathbf{L}_x\mathbf{N}_{,x} + \mathbf{L}_y\mathbf{N}_{,y} - jk\mathbf{L}_z\mathbf{N}\right]\{U^e\}\,e^{-j(kz-wt)} \\ &= \left[\mathbf{B}_1 - jk\mathbf{B}_2\right]\{U^e\}\,e^{-j(kz-wt)} \end{aligned} \tag{2.16}$$

where

$$\mathbf{B}_1 = \mathbf{L}_x\mathbf{N}_{,x} + \mathbf{L}_y\mathbf{N}_{,y} \tag{2.17}$$

$$\mathbf{B}_2 = \mathbf{L}_z\mathbf{N} \tag{2.18}$$

$\mathbf{N}_{,x}$ and $\mathbf{N}_{,y}$ are the derivatives of the shape function matrix with respect to x and y respectively. The shape function matrix and its derivatives are presented in Appendix A.

2.2.4 Displacement and strain variations

The variation of the displacement field in the x, y and z directions can be derived from equation 2.12 as:

$$\delta u = \delta u(x,y)e^{j(\kappa z - \omega t)} \tag{2.19}$$

$$\delta v = \delta v(x,y)e^{j(\kappa z - \omega t)} \tag{2.20}$$

$$\delta w = \delta w(x,y)e^{j(\kappa z - \omega t)} \tag{2.21}$$

Now using the definition of the strain-displacement relation in equations 2.7 and 2.8, the variation of strain is expressed as:

$$\delta\varepsilon = \left[\begin{Bmatrix} \frac{\partial \delta u}{\partial x} \\ \frac{\partial \delta v}{\partial y} \\ 0 \\ \frac{\partial \delta u}{\partial y} + \frac{\partial \delta v}{\partial x} \\ \frac{\partial \delta w}{\partial y} \\ \frac{\partial \delta w}{\partial x} \end{Bmatrix} + jk \begin{Bmatrix} 0 \\ 0 \\ \delta w \\ 0 \\ \delta v \\ \delta u \end{Bmatrix} \right] e^{j(kz - wt)} \tag{2.22}$$

Expressed in terms of the coefficient matrices $\mathbf{L}_x$, $\mathbf{L}_y$ and $\mathbf{L}_z$ as defined in 2.15, the strain variation becomes:

$$\delta\varepsilon = \left[\mathbf{L}_x \frac{\partial}{\partial x} + \mathbf{L}_y \frac{\partial}{\partial y} + \mathbf{L}_z \frac{\partial}{\partial z} \right] \delta\mathbf{u} \tag{2.23}$$

Using displacement shape functions, the nodal displacement variation is interpolated through the relation:

$$\delta\mathbf{u}(x,y,z,t) = \mathbf{N}\left\{\delta U^e\right\} e^{j(\kappa z - \omega t)} \tag{2.24}$$

Now substituting equation 2.24 into 2.23 leads to:

$$\begin{aligned} \delta\varepsilon &= \left[\mathbf{L}_x \mathbf{N}_{,x} + \mathbf{L}_y \mathbf{N}_{,y} + jk\mathbf{L}_z\mathbf{N}\right]\left\{\delta U^e\right\} e^{j(kz - wt)} \\ &= \left[\mathbf{B}_1 + jk\mathbf{B}_2\right]\left\{\delta U^e\right\} e^{j(kz - wt)} \end{aligned} \tag{2.25}$$

The transpose of the strain variation is given by:

$$\delta\varepsilon^T = \left\{\delta U^e\right\}^T \left[\mathbf{B}_1 + jk\mathbf{B}_2\right]^T e^{j(kz - wt)} \tag{2.26}$$

2.2.5 Equation of Motion

Using equations 2.9, 2.24 and 2.26, the first term of the variational statement in equation 2.11 is expanded as:

$$\begin{aligned}\int_V \delta\varepsilon^T \cdot \sigma dV &= \{\delta U^e\}^T \int_V \left[\mathbf{B}_1 + j\kappa\mathbf{B}_2\right]^T c\left[\mathbf{B}_1 - j\kappa\mathbf{B}_2\right] dV \{U^e\} \\ &= \{\delta U^e\}^T \int_V \left[\mathbf{B}_1^T c\mathbf{B}_1\right] - j\kappa\left[\mathbf{B}_1^T c\mathbf{B}_2\right] + j\kappa\left[\mathbf{B}_2^T c\mathbf{B}_1\right] + \kappa^2\left[\mathbf{B}_2^T c\mathbf{B}_2\right] dV \{U^e\} \\ &= \{\delta U^e\}^T \int_V \left[\mathbf{B}_1^T c\mathbf{B}_1\right] - j\kappa\left[\mathbf{B}_1^T c\mathbf{B}_2 - \mathbf{B}_2^T c\mathbf{B}_1\right] + \kappa^2\left[\mathbf{B}_2^T c\mathbf{B}_2\right] dV \{U^e\} \\ &= \{\delta U^e\}^T \left[\mathbf{K}_{11} - j\kappa\left(\mathbf{K}_{12} - \mathbf{K}_{21}\right) + \kappa^2\mathbf{K}_{22}\right] \end{aligned} \quad (2.27)$$

where

$$\mathbf{K}_{11} = \int_V \mathbf{B}_1^T c\mathbf{B}_1 dV \quad (2.28)$$

$$\mathbf{K}_{12} = \int_V \mathbf{B}_1^T c\mathbf{B}_2 dV \quad (2.29)$$

$$\mathbf{K}_{21} = \int_V \mathbf{B}_2^T c\mathbf{B}_1 dV \quad (2.30)$$

$$\mathbf{K}_{22} = \int_V \mathbf{B}_2^T c\mathbf{B}_2 \quad (2.31)$$

Using equations 2.13 and 2.12, the second term of equation 2.11 is expanded as:

$$\begin{aligned}-\omega^2 \int_V \rho\delta\mathbf{u}^T \cdot \mathbf{u} dV &= -\omega^2 \{\delta U^e\}^T \int_V \rho\mathbf{N}^T\mathbf{N} dV \{U^e\} \\ &= -\omega^2 \{\delta U^e\}^T \mathbf{M} \{U^e\} \end{aligned} \quad (2.32)$$

where

$$\mathbf{M} = \int_V \rho\mathbf{N}^T\mathbf{N} dV \quad (2.33)$$

The variational statement now becomes:

$$\{\delta U^e\}\left[\left(\mathbf{K}_{11} - j\kappa\left(\mathbf{K}_{12} - \mathbf{K}_{21}\right) + \kappa^2\mathbf{K}_{22}\right) - \omega^2\mathbf{M}\right]\{U^e\} = 0 \quad (2.34)$$

Since $\{\delta U^e\}$ is arbitrary, the equation of motion is:

$$\left[\left(\mathbf{K}_{11} - j\kappa\left(\mathbf{K}_{12} - \mathbf{K}_{21}\right) + \kappa^2\mathbf{K}_{22}\right) - \omega^2\mathbf{M}\right]\{U^e\} = 0 \quad (2.35)$$

The matrices K_{11}, K_{22} and M are all symmetric, while the K_{12} and K_{21}matrices are non-symmetric, making the entire system in 2.35 non-symmetric.

2.2.6 Solution of Free Vibration Problem

The guided wave solution to the free vibration problem is obtained by solving equation 2.35. The eigen-solution of the system may be solved for selected values of the wave number κ or the natural frequency ω, where either ω^2 or κ is computed as the eigen-value. Once the eigen-solution is available, the waves supported by the waveguide can be determined.

Eigenvalue problem in ω^2

When ω^2 is the eigenvalue of the problem, it is possible to solve the problem for selected values of κ that may be real, purely imaginary or complex. However, the former is commonly used since it recovers propagative waves that transport energy. The following text explains this.

If real values of κ are selected, equation 2.35 will be a real valued eigenvalue problem. The eigenvalues (ω^2) and corresponding mode shapes (ψ) will thus be real in nature, and the supported waves will be propagative. Propagative waves transport energy through the length of the waveguide. If κ is positive, the direction of propagation is forward, and for a negative κ the direction of wave propagation is backward. For a zero wave number, some eigen-values will be zero, corresponding to rigid body modes, while non-zero eigen-values correspond to cut-on frequencies.

For purely imaginary values of κ, the corresponding eigen-values and eigenvectors will be purely imaginary, [12]. The resulting wave forms are exponentially decaying near fields, and do not transport any appreciable mechanical energy, [12].

For complex values of κ, the eigen problem will be complex. The elastic wave will exponentially decay during propagation if the real and imaginary components have the same sign, otherwise, the wave will exponentially increase in magnitude while propagating [23].

Eigenvalue problem in κ

If the frequency is set and the wave number κ is now selected as the eigenvalue, equation 2.35 is rearranged as:

$$[A - \kappa B] \left\{ \begin{array}{c} U \\ \kappa U \end{array} \right\} = \left\{ \begin{array}{c} 0 \\ 0 \end{array} \right\} \tag{2.36}$$

where

$$A = \begin{bmatrix} K_{11} - \omega^2 M & 0 \\ 0 & -K_{22} \end{bmatrix} \; and \; B = \begin{bmatrix} j(K_{12} - K_{21}) & -K_{22} \\ -K_{22} & 0 \end{bmatrix} \tag{2.37}$$

The eigen problem in equation 2.36 is a non-symmetric complex valued problem. A complete set of modes (forward and backward propagating; exponentially decaying and exponentially increasing; and exponentially decaying and increasing while propagating) supported by the wave guide is now recovered.

2.2.7 Solution of Forced Vibration Problem

For a waveguide subjected to an external force F, the equation of motion in 2.36 now becomes:

$$[A - \kappa B] \left\{ \begin{array}{c} U \\ \kappa U \end{array} \right\} = \left\{ \begin{array}{c} F \\ 0 \end{array} \right\} \tag{2.38}$$

The solution to the forced response problem can be obtained by first taking the spatial Fourier transform of equation 2.38, [8, 20]. Thereafter, the solution to the resulting governing equation which is in the κ domain is written as an expansion in terms of eigenvectors, and finally the solution in the z domain is obtained by taking the inverse Fourier transform, [8].

The response of a waveguide at a distance z from the excitation point is therefore given by :

$$U(z) = \sum_{r=1}^{3N} \alpha_r \psi_r \tag{2.39}$$

where ψ_r is the eigenvector of mode r, and the term α_r is the modal amplitude evaluated as:

$$\alpha_r(z) = -j \frac{\psi_r^T F}{\psi_r^T B \psi_r} e^{-j\kappa_r z} \tag{2.40}$$

For a waveguide model with N degrees of freedoms, the eigen-solution in 2.36 results in $6N$ eigenvalue-eigenvector conjugate pairs. The solution in 2.39 is then computed from the $3N$ eigen values which are forward propagating, consisting of real and imaginary modes.

2.3 Free Vibration Characteristics of a Rail

The method described in Section 2.2 was implemented in MATLAB. The implementation followed that of Hayashi [14] and was performed as part of an independent study.

To compute the eigenvalues and associated vibrational mode shapes (eigen vectors) for a selected frequency range, equation 2.36 is adopted. The waveguide under consideration is a UIC60 rail modelled as an isotropic material with properties listed in Appendix B. The cross-section of the rail has a complex geometry which is symmetrical about the vertical axis. The 2D SAFE mesh of the rail cross-section is depicted in Figure 2.2. The model is discretized using fully integrated 4 noded quadrilateral elements. To achieve accurate results, the mesh was generated by following the rule of thumb of using at-least 10 elements per wavelength at maximum frequency of interest.

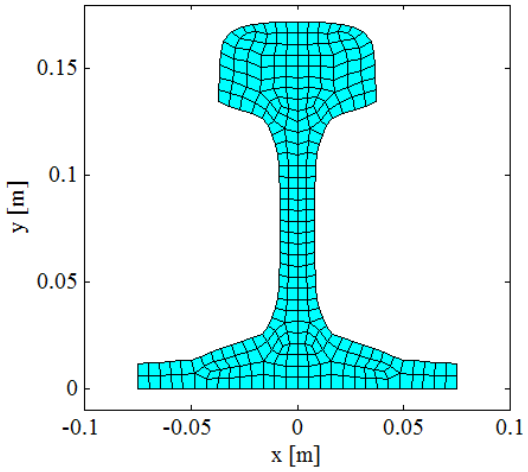

Figure 2.2: SAFE mesh of the rail

In guided waves, the expression in equation 2.36 is known as a dispersion relation. Dispersion is a phenomenon that describes how the speed of wave propagation in a medium varies with the natural frequency and the wave number. A wave form is said to be dispersive if the speed of wave propagation is dependent on the frequency, and thereby also dependent on the wave number. If the speed is independent of the frequency and the wave number, the wave form is said to be non-dispersive. Three types of dispersion curves used are the wave number plotted against frequency, the phase-velocity and group-velocity also plotted against the frequency axis.

Phase velocity is the velocity at which the phase of a wave mode with a particular frequency component travels. For the *nth* propagating mode, the phase velocity at frequency ω and wave number κ is expressed as:

$$v_{p,n} = \frac{\omega}{\kappa_n}. \tag{2.41}$$

Group velocity is the velocity at which the overall wave packet travels along the waveguide. By definition, group velocity is expressed as:

$$v_{g,n} = \frac{d\omega}{d\kappa_n} \tag{2.42}$$

Equation 2.42 can be evaluated by following the conventional approach or employing the theoretical formulae derived by Hayashi [14]. The conventional approach would require the solution of the eigen value problem to be sorted according to different modes of propagation as adjacent frequency points will be required to compute $^{\triangle\omega}/_{\triangle\kappa_n}$. The tracking of modes can be performed by following the sorting algorithm explained in [20], however the process becomes complicated when the modes cross each other or change from one form to another. The theoretical expression does not require the modes to be sorted. It is obtained by differentiating equation 2.35 with respect to frequency [5], and is given by:

$$v_{g,n} = \frac{1}{2\omega} \frac{\psi_n^T \left(K_{12} - K_{21} + 2\kappa_n K_{22}\right) \psi_n}{\psi_n^T M \psi_n} \tag{2.43}$$

The dispersion curves of the rail model are plotted in Figure 2.3. The curves show all the modes that are real and forward propagative below $50kHz$, with the web mode highlighted in red.

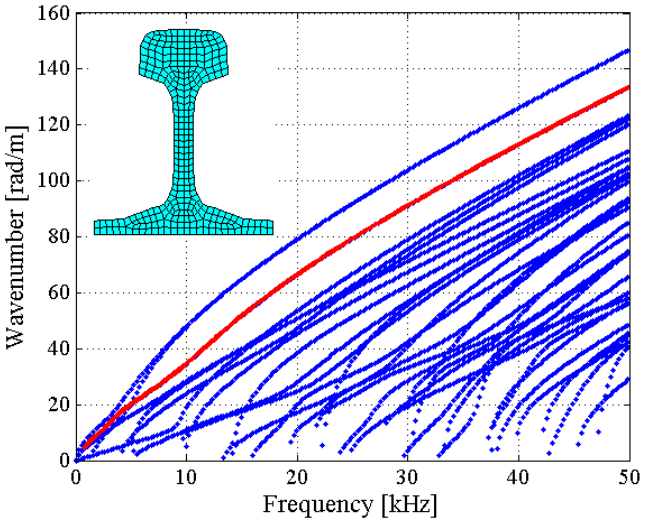

(a) Wave number

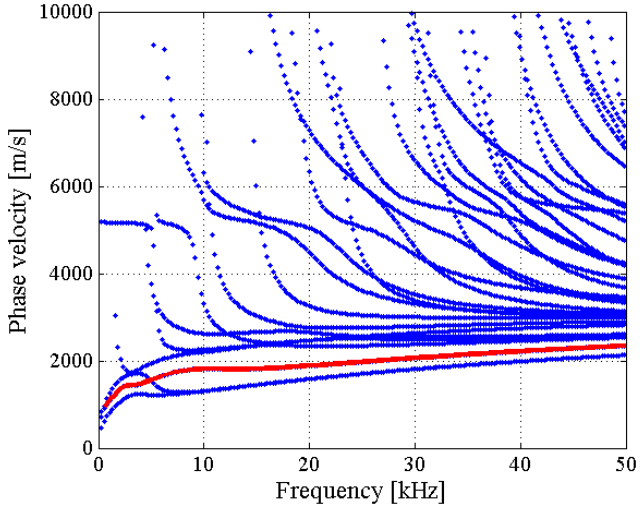

(b) Phase velocity

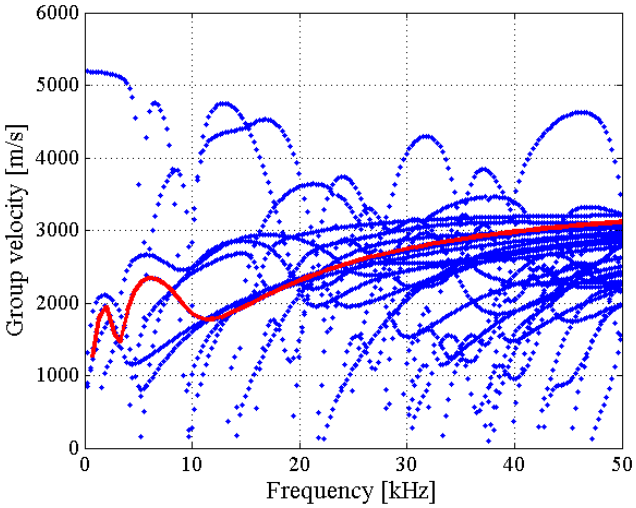

(c) Group velocity

Figure 2.3: Dispersion curves of the rail with the web mode highlighted in red (a) Wave number, (b) Phase velocity and (c) Group velocity

The phase velocity plot clearly shows that the web mode and three other modes are propagative for all excitation frequencies. These waves are said to have a zero cut-on frequency. The cut-on frequency is the frequency corresponding to a zero wave number. As the excitation frequency is increased, more wave modes start to propagate at their respective cut-on frequencies. Below their cut-on frequencies, the modes are non-real and are called evanescent modes [12].

The dispersion curves show that at low frequencies of propagation, the modes are highly dispersive as their phase and group velocities are constantly changing with frequency. However as the frequency becomes higher the modes become stable and thereby

less dispersive. It is seen from the curves that at $30kHz$ the web mode has a small dispersion. This characteristic makes the web mode a good candidate for defect detection since around this frequency and also at higher frequencies the velocity is almost constant indicating that the nature of the wave is subjected to almost a constant change with frequency. The mode shape plots showing the evolution of the web mode at several frequency points support this, Figure 2.4.

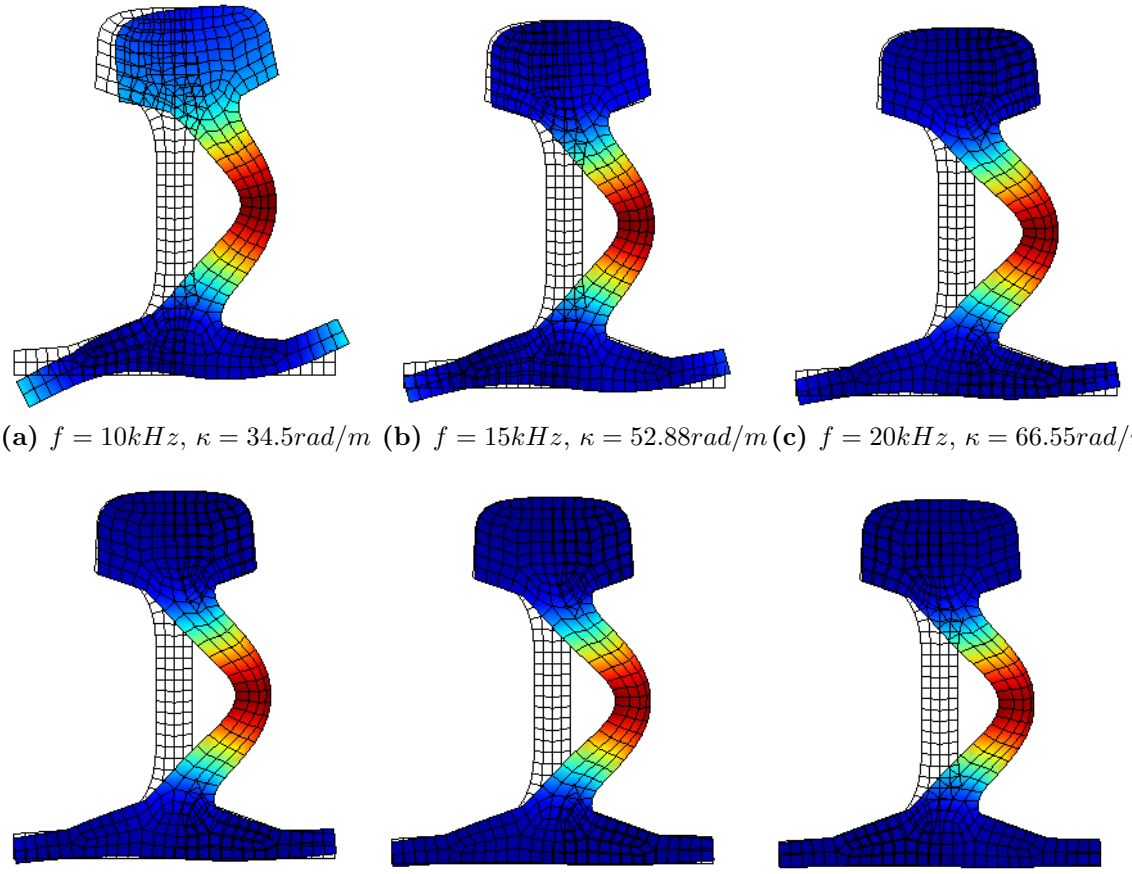

(a) $f = 10kHz$, $\kappa = 34.5rad/m$ **(b)** $f = 15kHz$, $\kappa = 52.88rad/m$ **(c)** $f = 20kHz$, $\kappa = 66.55rad/m$

(d) $f = 25kHz$, $\kappa = 80.0rad/m$ **(e)** $f = 30kHz$, $\kappa = 91.28rad/m$ **(f)** $f = 35kHz$, $\kappa = 102.35rad/m$

Figure 2.4: Web mode at different frequencies

Figure 2.4 shows that at $10kHz$ the web mode is not yet fully developed as an unacceptable fraction of energy is distributed to the foot and head of the rail. From $10kHz$ to $20kHz$, a sudden change in the distribution of energy is noticed. The foot and head sections start to undergo very small displacements while the web section continue to experience high displacements. At $25kHz$, the foot and head contain only a very small fraction of the wave energy which decreases gradually with an increase in frequency. At $35kHz$ the web mode is fully developed and the energy in the foot and head is hardly observed.

This section has demonstrated that the web mode is a good candidate for long range propagation and defect detection in the web at $f \gtrsim 30kHz$. In Section 2.4 it will be demonstrated that although performing the analysis at higher frequencies helps to avoid dispersion, it comes with a disadvantage of many modes of propagation being excited. This means that there is a possibility that an excitation of the web mode at higher frequencies might lead to a large portion of energy being transmitted to other modes of propagation.

2.4 Forced Response of a rail Web mode

The web mode was identified in the previous section. The plots illustrated that the mode is characterised by a horizontal movement of the web section, with the head and the foot subjected to almost no displacement. To excite the web mode, a horizontal point load is applied to a node at the centre of the web as shown in Figure 2.5.

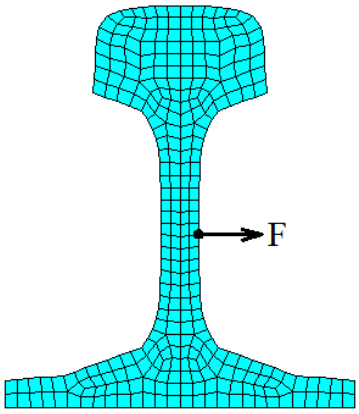

Figure 2.5: SAFE model of the rail subjected to a point load

The SAFE method is sensitive to the unrealistic modelling of the waveguide as undamped. The method can yield unstable results when the cut-on frequencies of propagating modes are excited. The effect of cut-on frequencies can sometimes be eliminated or reduced by adding damping to the waveguide model [5, 20], by filtering out the cut-on frequency points where the phase velocity curve become pseudo-vertical or alternatively by simply avoiding resonance frequencies and performing analyses at resonance-free frequency regions. In the implementation of the method, it was assumed that the waveguide is undamped. In this study, the third option is selected. It is thus critical to first determine resonance-free frequencies of analysis so that realistic results can be obtained. To achieve this, the rail web is excited with a uniform point load for all frequencies below

$45kHz$. Plotted in Figure 2.6 is the response of the rail (at the excited degree of freedom) per unit load as a function of frequency. The cut-on frequencies of all the modes propagating in this range are shown in the figure. The cut-on frequencies were solved from equation 2.35 for $\kappa = 0$.

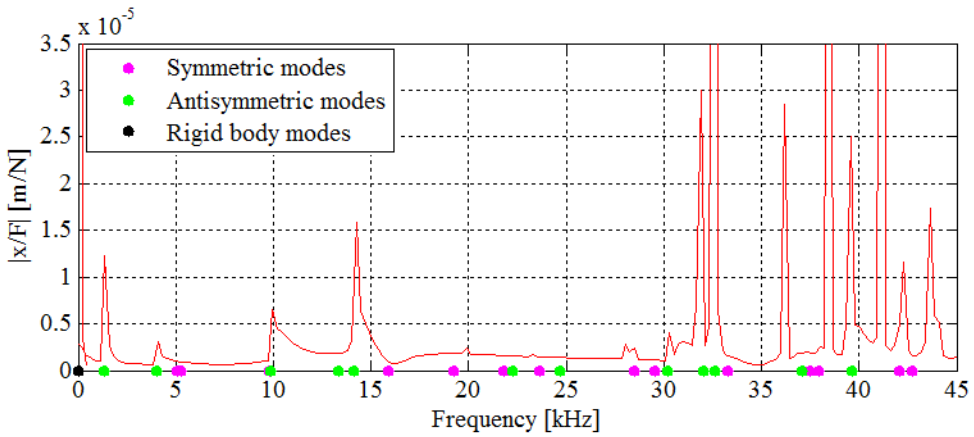

Figure 2.6: Frequency spectrum of the rail

Figure 2.6 shows that the frequency spectrum has peaks at certain frequencies. The figure shows that many of these resonance peaks correspond to cut-on frequencies of the anti-symmetric modes which we believe were excited by the point load. At higher frequencies, above $35kHz$, too many peaks are noticed. Some of the peaks (for instance, the first peak after $35kHz$) do not correspond to any cut-on frequency point. This now raises a question like "If it is not a cut-on frequency resulting in this resonance behaviour then what is it?", and calls for more research work on this topic. A number of frequency ranges suitable for the excitation of guided-waves can be identified from Figure 2.6. Some of these frequencies have a wide bandwidth (i.e at approximately 15-27kHz), whereas others have a narrow bandwidth (i.e at approximately 33-36kHz).

To now illustrate the significance of first determining resonance free-frequencies for the undamped case, the forced response problem of the rail web is studied at frequencies around $24kHz$ and $30kHz$ respectively. The rail is forced with a $10.5\,cycle$ Hanning windowed tone burst centred respectively at $24kHz$ and $30kHz$. The two excitation signals are plotted in the time and frequency domains in Figure 2.7.

To evaluate the accuracy of the SAFE results, the forced response problem was also solved in ABAQUS explicit. The ABAQUS model is as depicted in Figure 2.8. The force and receiver points are located in the middle of the model away from the free-ends to avoid reflections from the boundaries.

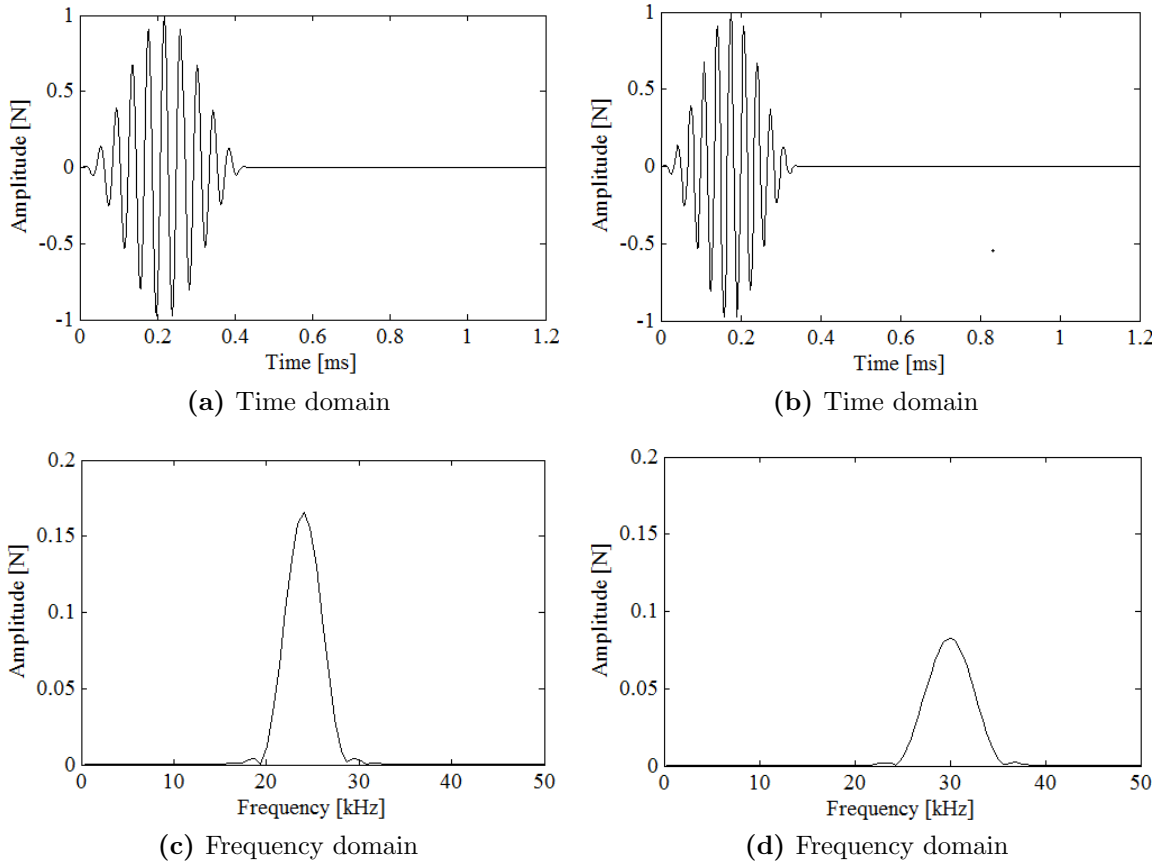

(a) Time domain **(b)** Time domain

(c) Frequency domain **(d)** Frequency domain

Figure 2.7: Excitation signals at (a) & (c) $24kHz$ and (b) & (d) $30kHz$ centre frequencies

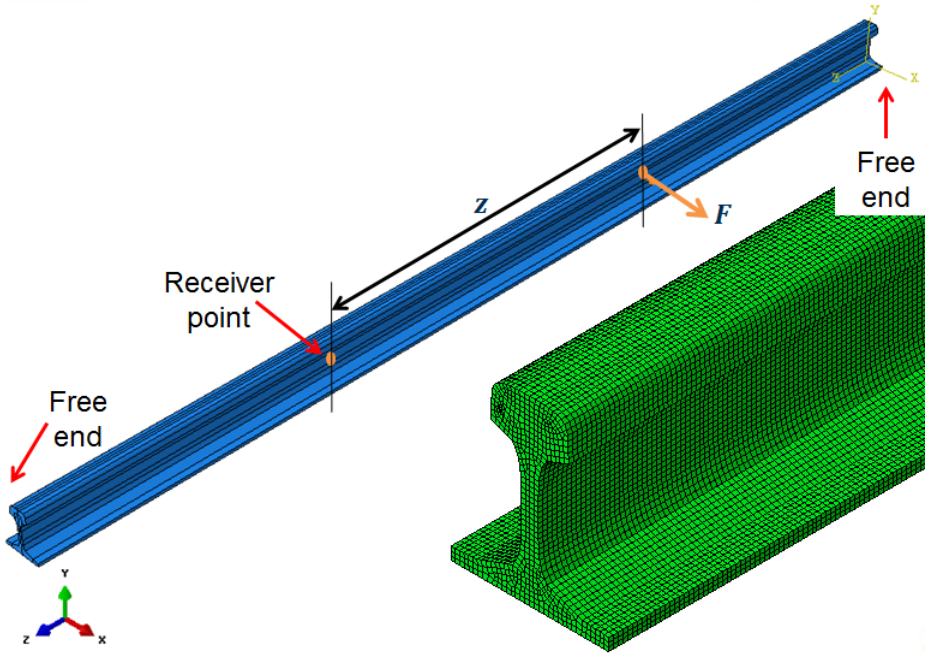

Figure 2.8: ABAQUS model of the forced response problem

The results obtained from SAFE and ABAQUS are compared in Figure 2.9. The responses were computed at a distance of $z = 1m$ away from the excitation point.

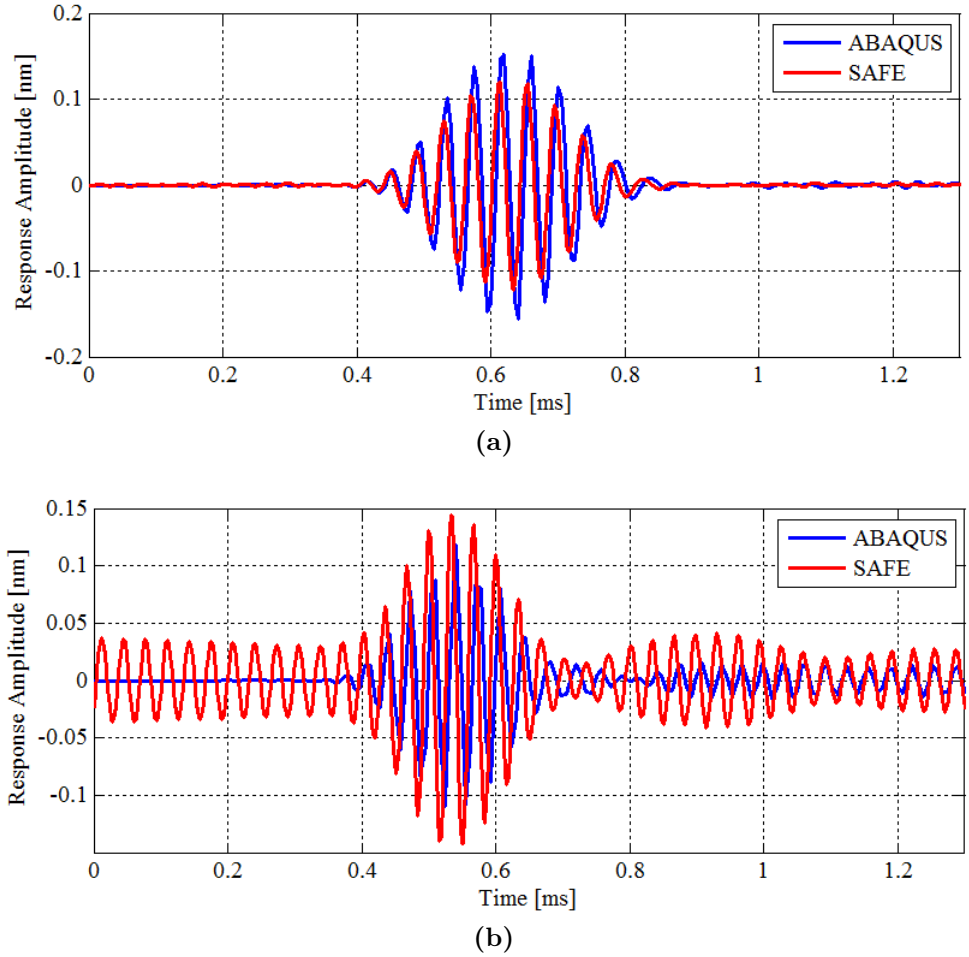

Figure 2.9: Response of the rail under a point load excitation at (a)$24kHz$ and (b)$30kHz$

The results for $24kHz$ excitation show that within a period of $1.2ms$, only one wave packet was detected at the receiver point. This suggests that when excited at this frequency, the web mode is excited and propagates along the rail while other modes are not excited. The correlation between SAFE and ABAQUS in Figure 2.9a is good. Only a slight difference in the response amplitude is encountered.

When the rail is excited at $30kHz$, the results from ABAQUS and SAFE are different. The SAFE results predict that immediately after excitation, the rail web is already experiencing wave motion $1m$ away from the source. This prediction is obviously not realistic since a wave form must travel for some time before reaching the receiver point. The prediction from ABAQUS that the web mode takes approximately $0.4ms$ to arrive at the source location is acceptable. SAFE was able to predict the web mode, however the response amplitude is now over estimated since the unrealistic component is added

to the response. The existence of the unrealistic component is due to the excited resonance frequencies just after $30kHz$ in Figure 2.6. The response of the rail plotted in the frequency domain in Figure 2.10 explains this clearly. The frequency response is smooth for $24kHz$ excitation while it contains some resonance peaks for $30kHz$ excitation.

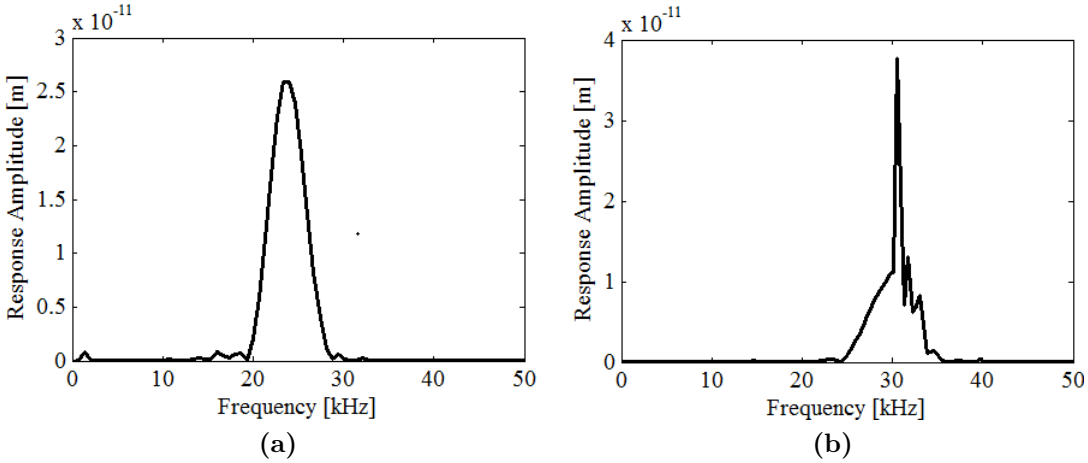

Figure 2.10: Response signals in the frequency domain at (a)$24kHz$ and (b)$30kHz$

An illustration of the web mode propagating through the rail at $24kHz$ is shown in Figure 2.11.

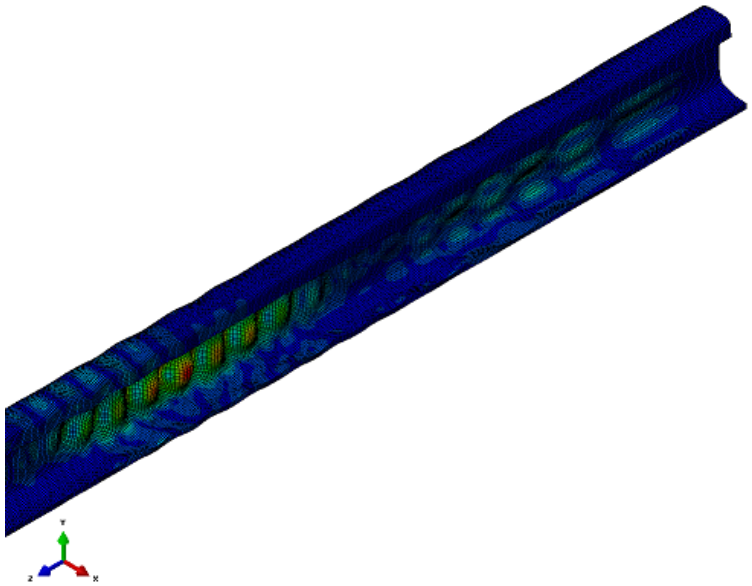

Figure 2.11: Web mode propagation at $24kHz$ excitation - ABAQUS

2.5 Conclusion

The purpose of this chapter was to introduce the SAFE method and use it to study a forced response problem of the web mode while highlighting one of its drawbacks. The

web mode was identified as a propagative mode with energy concentrated in the web of the rail. The mode is highly dispersive at lower frequencies and become less dispersive as the frequency increases. The forced response problem revealed that under the assumption that the waveguide model is undamped, the resonance frequencies (associated with cut-ons) yield unrealistic results when excited. Good frequencies of analysis were therefore identified, one in the vicinity of $24kHz$ and the other around $35kHz$. It was demonstrated that when an undamped analysis is performed within the good frequency regions, the SAFE method and ABAQUS yield similar results indicating that the method was correctly implemented and is accurate.

The main goal of this study is to design a piezoelectric transducer that operates at the operational frequency of the UBRD system, which is $35kHz$. Since this operational frequency falls within a good frequency region of analysis, it can be deduced that the cut-on effects can be avoided without having to implement the other methods mentioned in Section 2.4 to counteract the resonance problem.

CHAPTER 3

Modelling of a Piezoelectric Transducer Attached to a Wave Guide Using the SAFE-3D Method

It was demonstrated in the previous chapter that the SAFE method can be trusted if correctly implemented and when the analysis is carried out in the resonant-free frequency regions for no damping assumption. In this chapter, the SAFE method together with the traditional finite element method are employed in a recently developed method called SAFE-3D. In the SAFE-3D method, the wave guide, which is a rail track in this study, is modelled using a 2D SAFE mesh and the piezoelectric transducer is modelled using 3D finite elements. The objective of this chapter is to introduce the SAFE-3D method to the reader and verify that the method accurately predicts the excitation of guided waves by a transducer. An available transducer is used to study the excitation of guided waves in the rail web at the operational frequency ($35kHz$) of the UBRD system.

3.1 Modelling of a Piezoelectric Transducer

3.1.1 Piezoelectricity

Piezoelectricity refers to a phenomenon whereby a material generates an electric potential when subjected to mechanical stress, or conversely, the material undergoes mechanical deformation due to an applied electric field [16]. These two reversible effects are respectively referred to as the direct and indirect piezoelectric effects [25]. A piezoelectric material have both mechanical and electrical properties.

The piezoelectric effect is assumed to be linear, and occurs only in anisotropic materials. The constitutive equations governing the direct and indirect piezoelectric effect are respectively given by [27]:

$$\begin{aligned} \mathbf{D} &= \mathbf{eS} + \boldsymbol{\epsilon}^S \mathbf{E} \\ \mathbf{T} &= \mathbf{c}^E \mathbf{S} - \mathbf{e}^t \mathbf{E} \end{aligned} \tag{3.1}$$

where the mechanical variables are the stress vector $\mathbf{T}$ and the strain vector $\mathbf{S}$, and the electrical variables are the dielectric displacement vector $\mathbf{D}$ and the electric field vector $\mathbf{E}$. The matrix $\mathbf{c}^E$ is the stiffness of the material under constant electric field, $\mathbf{e}$ is the piezoelectric constant matrix and ϵ^S is the electrical permittivity under constant strain. The superscript t denotes a transposed matrix.

Piezoelectric ceramic materials are orthotropic. Polling the material will result in the piezoelectric becoming transversely isotropic, with a rotational symmetry around the direction of polarization [33]. When the polling is in the $z-direction$ (33 direction), the equations in 3.1 are expanded as:

$$\begin{bmatrix} D_1 \\ D_2 \\ D_3 \end{bmatrix} = \begin{bmatrix} 0 & 0 & 0 & 0 & e_{15} & 0 \\ 0 & 0 & 0 & e_{24} & 0 & 0 \\ e_{31} & e_{32} & e_{33} & 0 & 0 & 0 \end{bmatrix} \begin{bmatrix} S_1 \\ S_2 \\ S_3 \\ S_4 \\ S_5 \\ S_6 \end{bmatrix} + \begin{bmatrix} \epsilon_{11}^S & 0 & 0 \\ 0 & \epsilon_{22}^S & 0 \\ 0 & 0 & \epsilon_{33}^S \end{bmatrix} \begin{bmatrix} E_1 \\ E_2 \\ E_3 \end{bmatrix} \tag{3.2}$$

$$\begin{bmatrix} T_1 \\ T_2 \\ T_3 \\ T_4 \\ T_5 \\ T_6 \end{bmatrix} = \begin{bmatrix} c_{11}^E & c_{12}^E & c_{13}^E & 0 & 0 & 0 \\ c_{21}^E & c_{22}^E & c_{23}^E & 0 & 0 & 0 \\ c_{31}^E & c_{32}^E & c_{33}^E & 0 & 0 & 0 \\ 0 & 0 & 0 & c_{44}^E & 0 & 0 \\ 0 & 0 & 0 & 0 & c_{55}^E & 0 \\ 0 & 0 & 0 & 0 & 0 & c_{66}^E \end{bmatrix} \begin{bmatrix} S_1 \\ S_2 \\ S_3 \\ S_4 \\ S_5 \\ S_6 \end{bmatrix} - \begin{bmatrix} 0 & 0 & e_{31} \\ 0 & 0 & e_{32} \\ 0 & 0 & e_{33} \\ 0 & e_{24} & 0 \\ e_{15} & 0 & 0 \\ 0 & 0 & 0 \end{bmatrix} \begin{bmatrix} E_1 \\ E_2 \\ E_3 \end{bmatrix} \tag{3.3}$$

where $c_{66}^E = \frac{1}{2}\left(c_{11}^E - c_{12}^E\right)$.

Equation 3.2 is the basis for the formulation governing a piezoelectric sensor while equation 3.3 is that for an actuator [25].

3.1.2 Finite Element Modelling

In this study, the 3D traditional finite element method is used for modelling the piezoelectric transducer. The formulation of the method will only be briefly explained in this section since the method is well known. A detailed explanation can be found in the textbooks of [7, 35] and also in references [26] and [10].

The finite element dynamic equations governing the piezoelectric behaviour can be derived from Hamilton's principle by employing the strain energy, kinetic energy, electrostatic energy and the virtual work relations; such that the electrical as well as mechanical contributions are included in the formulation. The transducer model is discretized by using fully integrated 8-noded brick elements referred to as hexahedral elements. Each node has three mechanical degrees of freedom (displacement) and one electrical degree of freedom (electric potential/voltage). The element displacement field and electrical potential are related to the corresponding nodal values by using shape functions, while the strain and electric fields are respectively related to the nodal displacements and potential by the shape function derivatives [26].

The dynamic equations for a piezoelectric medium are given by:

$$\begin{bmatrix} K_{uu} - \omega^2 M & K_{u\phi} \\ K_{u\phi}^T & K_{\phi\phi} \end{bmatrix} \begin{Bmatrix} u \\ \phi \end{Bmatrix} = \begin{Bmatrix} f \\ q \end{Bmatrix} \tag{3.4}$$

where K_{uu} is the mechanical stiffness, $K_{u\phi}$ is the electromechanical matrix and $K_{\phi\phi}$ is the electric capacitance matrix. The variables u and ϕ are respectively the mechanical displacement and electric potential, while f and q are the applied mechanical force and electrical charge, respectively.

A finite element model of a typical piezoelectric transducer considered in this Chapter is shown in Figure 3.1.

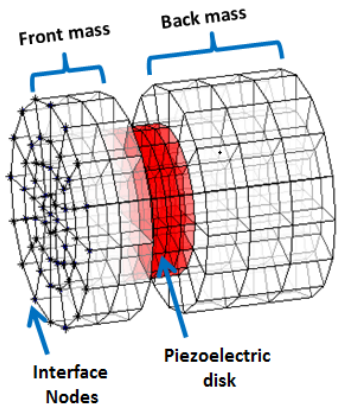

Figure 3.1: A typical piezoelectric transducer

The transducer consist of two steel masses sandwiched between a piezoelectric stack. To use the transducer for guided wave excitation, actuation is achieved by imposing a voltage across the electrodes of the piezoelectric stack. The nodes on the transducer referred to as the interface nodes, are highlighted in the Figure. Interface nodes are the nodes on the front face of the transducer, used to attach the transducer to a waveguide model in the SAFE-3D method.

3.2 The SAFE-3D Method

The SAFE-3D method employs a 2D cross-sectional mesh of the waveguide and a 3D mesh of the transducer. The transducer is attached to the desired location on the waveguide model through the interface nodes, with the aim to excite specific modes of propagation.

The modelling of guided wave excitation in the SAFE-3D method encompasses five key procedure steps. With the two sets of system matrices computed from SAFE and 3D FEM available, it is first convenient to compute the finite element nodal interaction matrix between the SAFE model and the 3D model, where the transducer is in contact with the waveguide. This is significant particularly in the case of non-coincident nodes, where the interaction matrix is required to effectively interpolate and map model data between the waveguide and transducer models. Secondly, the receptance matrix, and therefore the dynamic stiffness of the waveguide section in contact with the transducer are constructed. This procedure step entails computing the response of the rail contact degrees of freedom to unit excitation forces. Modal amplitudes of waves propagating though the waveguide due to the unit excitation forces are also computed at this stage. Thereafter, the dynamic stiffness of the waveguide is added to the stiffness of the transducer in order to impose the boundary condition constraint experienced by the transducer due to the waveguide structure. The transducer harmonic response problem can then be solved to determine the displacements of the interface nodes and the actual forces applied to the waveguide. In the fourth key procedure step, the computed modal amplitudes due to unit forces are scaled with the actual forces. Finally, the waveguide time response at the desired output distance from the point of excitation can be constructed. A process flow chart of the SAFE-3D method analysis procedure is presented in Figure 3.2. The details of the key procedure steps are presented next.

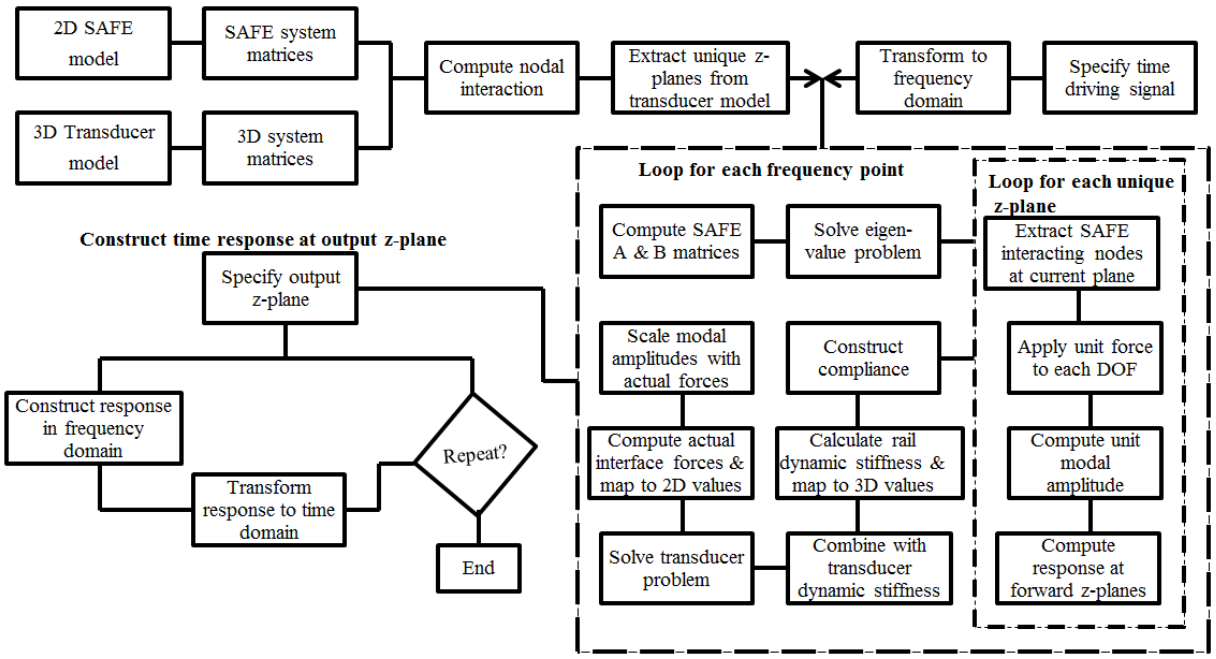

Figure 3.2: Process flow chart of the SAFE-3D method

The SAFE model has nodes only at the plane $z = 0$, whereas the transducer has nodes at different $z-planes$ since the model is in 3D. The unique $z-planes$ of the 3D interface nodes (in contact with the SAFE mesh) are identified. Treating the length terms in the SAFE model analytically, the corresponding SAFE interface nodes interacting with each of the 3D interface nodes are identified. A nodal interaction matrix of dimension $[h \times l]$ (where h and l are respectively the number of 3D and SAFE interface nodes), consisting of components ranging between zero and one is calculated. The number one signifies a complete interaction between a 3D node and the SAFE node, meaning that the nodes are coincident. The interaction matrix is computed using the isoparametric shape functions.

The response of the waveguide to applied loads is computed using equation 2.39. The applied forces and displacement response are related to the waveguide receptance matrix R_w through:

$$U_{in} = R_w F_{in} \tag{3.5}$$

where U_{in} and F_{in} respectively denotes the displacement and input forces at the SAFE interface DOFs. The dynamic stiffness matrix D_w of the waveguide is defined as the inverse of the receptance matrix, and is given by:

$$D_w U_{in} = F_{in} \tag{3.6}$$

For a sandwich transducer, the contact face contain only mechanical properties. The mechanical dynamic stiffness of the transducer is thus extracted from equation 3.4 as:

$$[D_T]\{u\} = \left[K_{uu} - \omega^2 M\right]\{u\} = \{f\} \tag{3.7}$$

The dynamic stiffness of the transducer can be partitioned into DOFs in contact with the rail (in) and DOFs not in contact (n). The dynamic stiffness of the rail experienced by the transducer is interpolated to 3D values using the interaction matrix, and then added to the dynamic stiffness of the transducer interface nodes:

$$\begin{bmatrix} D_{T,nn} & D_{T,nin} \\ D_{T,inn} & D_{T,inin} + \tilde{D}_w \end{bmatrix} \begin{Bmatrix} u_n \\ u_{in} \end{Bmatrix} = \begin{Bmatrix} f_n \\ f_{in} \end{Bmatrix} \tag{3.8}$$

where $\tilde{D}_w$ indicates that the waveguide dynamic stiffness is now mapped to the 3D space.

Now to take into account the full electro-mechanical coupling in the transducer model, the effective dynamic stiffness from equation 3.8 is substituted back in equation 3.4 for $[K_{uu} - \omega^2 M]$ and the unknown transducer displacements and actual interface forces are computed for an applied electrical potential. The actual interface forces computed from the 3D model are mapped to the SAFE model by employing the interact matrix, and then used to scale the modal amplitudes of the waveguide. Finally, with the waveguide model now subjected to the actual transducer forces, the response of the waveguide at the desired location from the excitation point can be computed.

3.3 Web Mode Excitation with a Transducer using the SAFE-3D Method

In this chapter, an available transducer (depicted in Figure 3.1) is attached to the web section of the UIC60 profile rail through non-coincident nodes. The piezoelectric disk is subjected to a linear voltage field varying from $0V$ at the face in contact with the back mass to $1V$ at the other face. The interface nodes, through which the transducer model will be attached to the rail model, are highlighted in Figure 3.1. With the interface nodes constrained, the static deformation of the transducer is as depicted in Figures 3.3.

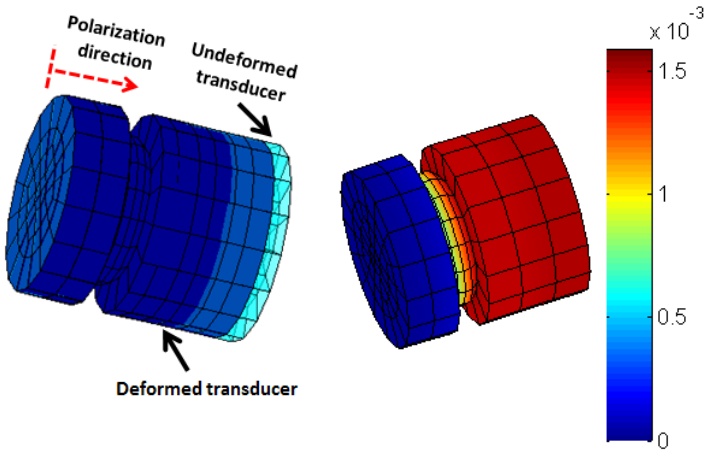

(a) Undeformed and deformed bodies

(b) Displacement field

Figure 3.3: Displacement deformation of the transducer.

The application of the SAFE-3D method to excite the web mode using a transducer is illustrated in Figure 3.4.

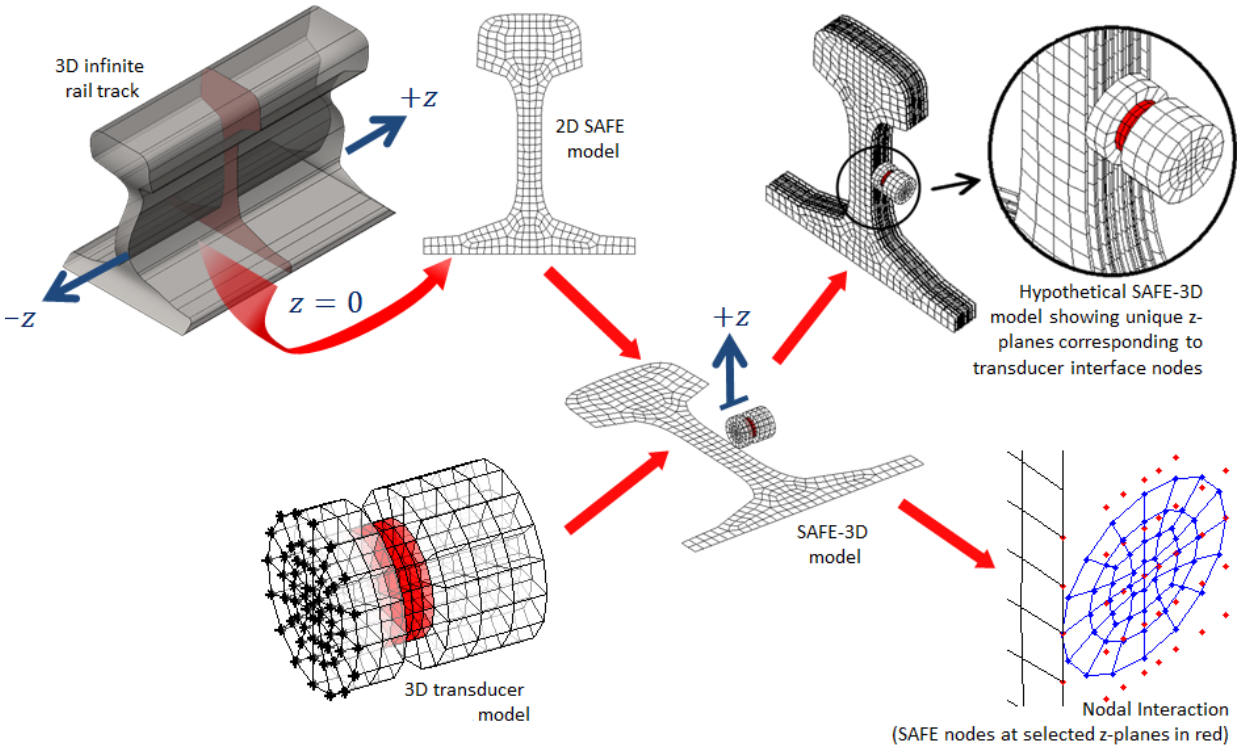

Figure 3.4: Excitation of the web mode using a piezoelectric transducer in the SAFE-3D method.

The piezoelectric transducer is attached to the web of the rail. The identified unique z-planes corresponding to the 3D interface nodes are shown in a hypothetical SAFE-3D model in the Figure.

For the analyses in this Chapter, the frequency ranges at $24kHz$ and $35kHz$ in Figure 2.6 were selected. To avoid the effect of cut-on frequencies by performing the analysis within the narrow bandwidth at $35kHz$, a tone burst signal with a high number of cycles was used for this frequency. The transducer was respectively driven with a $24kHz$ and $35kHz$ centre frequency Hanning windowed tone burst signals with 10.5 and 17.5 cycles, respectively.

3.4 Validation of the SAFE-3D method

The validate the accuracy of the SAFE-3D method, experimental measurements were carried out in the lab. The transducer was bonded to the web of an available $5m$ long UIC60 rail segment, located at a distance of $1.5m$ from one end. The experimental measurement was carried out using a 17.5 cycle hanning-windowed tone-burst at $35kHz$ excitation. The unit amplitude voltage signals across the 4 piezoelectric disks were amplified to a peak amplitude of $20Volts$. The horizontal displacement response at the centre of the rail web was measured at a $1.5m$ distance from the transducer location. A Polytec PSV-400 laser vibrometer was used to perform this experimental measurement. The output displacement was then scaled by a factor of $1/80$ to compare with modelling results from SAFE3D, where a $1V$ peak amplitude excitation signal was used.

The results obtained respectively at $24kHz$ and $35kHz$ excitations are compared to SAFE-3D results in Figure 3.5.

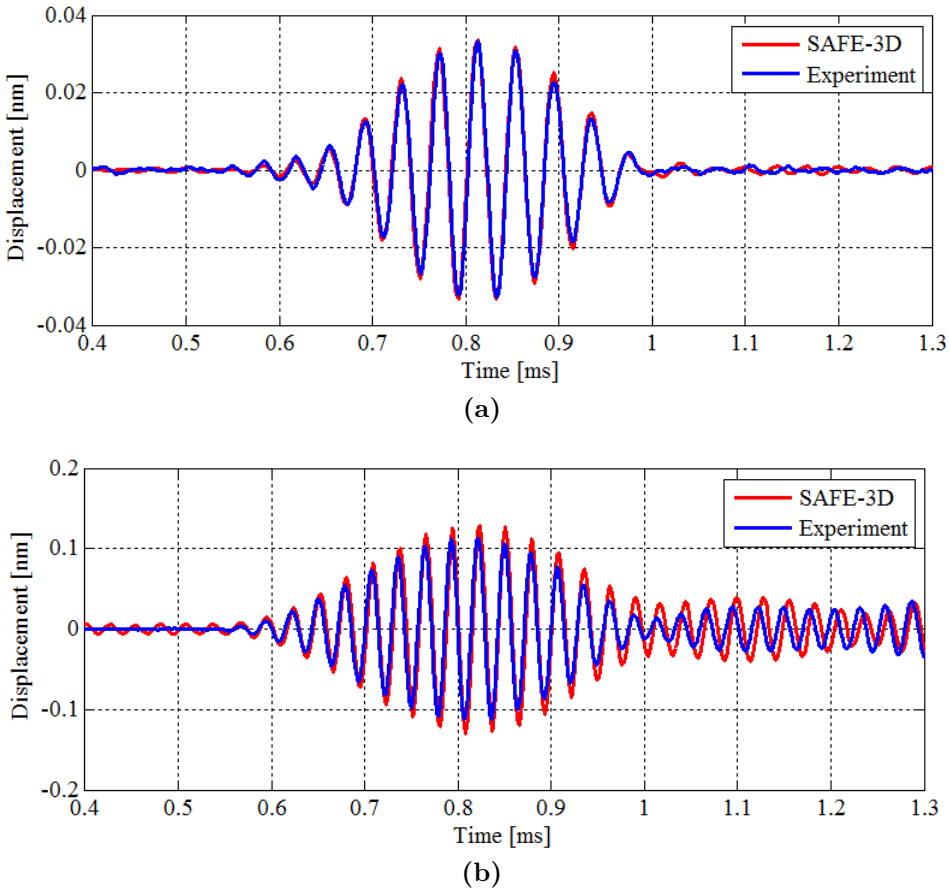

Figure 3.5: Response of the rail excited by a piezoelectric transducer driven at (a) $24kHz$ and (b) $35kHz$.

The results for the two analyses demonstrate an exceptional agreement between SAFE-3D and the experimental measurements. The selected frequency ranges are therefore good for guided wave modelling of the undamped rail.

3.5 Conclusion

This chapter has demonstrated the analysis of a piezoelectric transducer attached to a rail waveguide using the recently developed SAFE-3D method. In the SAFE-3D method, a 2D SAFE mesh of the waveguide as well as a 3D FEM mesh of a piezoelectric transducer were employed. The interaction between the two models was computed, and used to map and interpolate model information between SAFE and 3D FEM models. The analysis was performed at good frequencies to avoid the effect of cut-on frequencies as damping was not added to the waveguide model. The results obtained from the SAFE-3D method were found to be in good agreement with experimental measurements. The validity of results reveals that for an undamped model, the method yield good results when the cut-on frequency points are avoided in the analysis. The method can therefore be employed in the design process of a piezoelectric transducer for exciting the web mode. The optimal

design of the transducer using mathematical optimization is described in Chapter 4.

CHAPTER 4

Design Optimization of a Piezoelectric Transducer to Excite Guided Waves in a Rail Web

As it was verified in the previous chapter, the SAFE-3D method is accurate and therefore suitable for use in designing the piezoelectric transducer required for the UBRD system. As already stated, the transducer will be integrated into the system so as to upgrade its functionality to detect cracks in the web section of the rail. The major requirement of the design is for the transducer to strongly excite the web mode at a frequency of $35kHz$. This implies that the performance of the transducer needs to be optimized at this frequency. This chapter aims to find the optimized design of the transducer by using numerical modelling, Design of Experiments (DoE) and optimization methods.

4.1 Introduction

Design optimization is the process of searching for an alternative design with the highest achievable performance by maximizing desired factors and minimizing cost and other undesired factors. The optimization of a design is an iterative process and primarily requires the evaluation of many alternatives subjected to different input parameters until an acceptable design is obtained within a defined domain. The three possible methods that can be adopted to evaluate multiple designs and optimize performance are the:

1. trial and error field or laboratory optimization,
2. trial and error numerical optimization, and

3. rigorous numerical optimization.

Trial and error optimization methods are traditional approaches that involve conducting a series of experiments by changing the input parameters one at a time, until there is no further improvement of a design performance measure. In a case where the design space is multidimensional, these approaches can be ineffective, especially when the experimenter lacks experience, as the manner in which the input parameters are varied is not formally controlled. Changing one parameter at a time can make it difficult to identify the real optimum, in particular when the problem is multi-modal as different starting points may result in different solutions. A serious drawback with trial and error methods is that they can be costly and time consuming to carry out. The field and laboratory experiments may accumulate manufacturing costs as every trial design needs to be manufactured. Another point worth noting is that conducting field and laboratory experiments can be time consuming as the process is carried out by man and cannot be automated.

On the other hand, the trial and error numerical optimization method replaces physical experiments by simulated experiments. Hence the evaluation of a trial design is automated but the decision of which trial design to consider next is still carried out by the designer. The process is still driven manually although each iteration is more efficient. Trial and error methods if not carefully conducted may not provide conclusive information about the design and its influential factors. Trial and error approaches are intuitively driven, and that may severely influence the direction based on the design engineers experience.

Rather than using laborious trial and error methods, the best alternative is to adopt a carefully conducted numerical optimization approach that is properly and consistently formulated. By formalizing the design approach we are not only better enabled to provide a desired answer, but our understanding of the problem may be enhanced. In the formal numerical optimization method, the input design parameters are not only varied simultaneously but also systematically over the design domain. An advantage of this method is that the process can be automated to free the design engineer's time. If the method is well implemented in a computing system, it is not subject to any human bias, and better results can be achieved due to a high level of control of input parameters and the strictly imposed conditions.

Proper formulation of a design optimization problem is critical as it determines the set of designs to choose from as well as quantifies the differences between designs. The optimization formulation procedure can be divided into five main steps [4]:

Step 1: **Problem description**. The statement describes the objectives of the design problem and the requirements to be met.

Step 2: **Data and information collection**. Information on factors such as material properties, performance requirements and resource limits need to be gathered. Analysis procedures and tools must also be identified.

Step 3: **Definition of design variables**. A set of variables describing the design system.

Step 4: **Optimization criterion**. A design performance measure used to quantitatively compare different designs and designate one as better than another. Such a criterion is referred to as an objective function.

Step 5: **Formulation of constraints**. The restrictions placed on the design that determines the set of designs available as candidate solutions. If we forget to include a critical constraint in the formulation, the optimum solution will most likely violate it. Also if we have too many constraints, or if they are inconsistent, there may be no solution.

The optimization formulation for designing a rail web transducer is presented next.

4.1.1 Optimization formulation for the design of a rail web transducer

Step 1: Problem description The goal is to design a piezoelectric transducer to excite ultrasonic guided waves in the web section of a rail. The transducer should be of a sandwich type and have a structural configuration as illustrated in Figure 4.1. The resonator of the transducer should consist of four piezoelectric ceramic disks and two sets of brass electrodes connecting surfaces of the same potential. The system will be assembled together using a pre-stressed bolt.

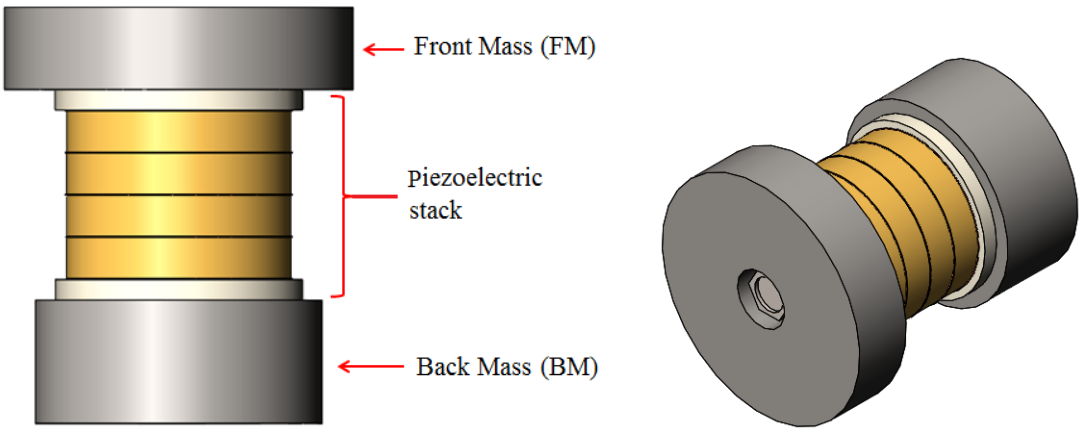

(a) Side view **(b)** Isometric view

Figure 4.1: The structural configuration of a typical piezoelectric transducer

It is required that the transducer must strongly excite a rail web mode when driven by a $35kHz$ centre frequency hanning-windowed tone burst signal. Thus, the objective is to maximize the amount of energy that the transducer can transmit to the web mode under the proposed operational frequency conditions.

Step 2: Data and information collection

Material properties The front and back sections of the transducer each comprise a steel mass. The material properties are tabulated in 4.1.

Table 4.1: Material properties of the transducer

Property	Value
Steel	
Youngs' Modulus, $[GPa]$	210
Density, $[kg/m^3]$	7800
Poison's Ratio	0.3
Properties for Type IV PZT are listed in Appendix B.	

Geometrical properties For this study, the main interest in the design problem is to evaluate the effect of the sizes of the steel masses on transducer performance. It is for this reason that the piezoelectric stack (as highlighted in Figure 4.1) will be kept constant as none of these components are regarded as design variables. The dimensions of the piezoelectric stack are not disclosed due to intellectual property considerations at the CSIR.

Resource limits To minimise the cost of resources required for the transducer, the choice of materials used was based on what was available at the CSIR. A Type IV PZT was selected amongst the available types of piezoelectric ceramics at the CSIR. Table B.2 in Appendix B list the material properties of PZT IV. A Type IV PZT was selected due to its good piezoelectric properties. It has the highest charge constant d, and the lowest voltage constant g, making its relative dielectric constant high. The dielectric constant is a measure of the ability of the material to store electrical energy in an electric field. The relative dielectric constant is defined as:

$$K = \frac{e}{\varepsilon_0} = \frac{d}{g\varepsilon_0}, \tag{4.1}$$

where e is the permittivity of the material and ε_0 is the permittivity of free space.

Analysis procedure and analysis tools To analyse the performance of trial transducer designs, the SAFE3D method will be employed. The 3D FEM transducer design model will be attached to the web of the 2D SAFE rail model. A hanning-windowed tone burst voltage signal centred at $35kHz$ will be used to drive the transducer model. The web mode response of a horizontal degree of freedom at the web centre will then be evaluated and used to estimate the amount of energy that the transducer transmitted to the web mode. The analysis of the combined 3D FEM transducer and 2D SAFE rail models was discussed in detail in Chapter 3.

Step 3: Definition of design variables To allow for the use of an available transducer housing, a decision was made to keep the diameter of the front mass constant, at a size compatible with the housing. The diameter of the front mass shall thus be fixed at $17mm$. The design problem therefore contains only three design variables; the thickness of the front mass (FM), the thickness of the back mass (BM) and the diameter of the back mass. Although fixing the diameter of the front mass poses a limitation on the design problem, it provides notable advantages which include: reduced problem complexity and improved computational cost and time.

Step 4: Optimization criterion When a piezoelectric transducer is attached to a rail to excite the rail's guided waves, all the modes of propagation supported by the rail can be excited. The magnitude with which each mode is excited is dependant on the location of the transducer on the rail and described by a factor referred to as the modal amplitude (discussed in Chapters 2 and 3). The modal amplitude captures the dynamics of the transducer very well when the actual energy put into the rail is not scaled, which is our situation. The modal amplitudes of the web mode for three typical transducer designs are plotted in Figure 4.2a. It is seen from the figure that the function is not well behaved as it has abrupt bends at certain frequencies due to the effect of resonance as explained in Section 2.4. Although the function captures the dynamics of the transducer well, it is not advised to be used as an optimization criterion as it is not smoothly continuous.

From the modal amplitudes, the frequency response function of the rail can be computed by summing all the propagating modes of interest based on their modal participation factors. Since the interest of the design problem is on the web mode, the frequency response function must be based on only the web mode for performance characterisation purposes. The frequency response function for the three typical transducer designs are plotted in Figure 4.2b. The function is scaled by a tone burst signal used to drive the transducer model. The time history of the web mode can be computed by taking the inverse Fast Fourier transform of the frequency response function.

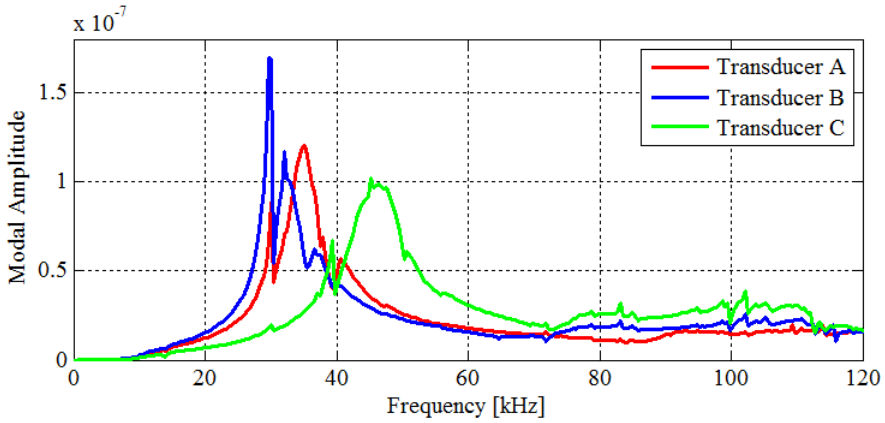

(a) Modal Amplitude of the web mode

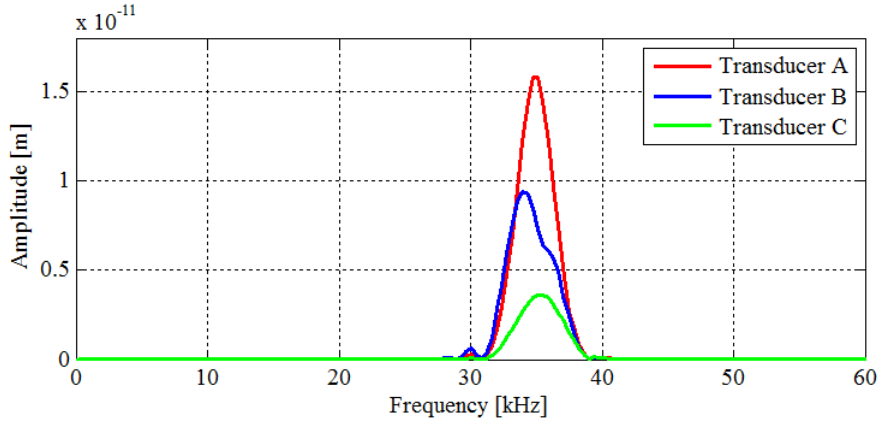

(b) Frequency response

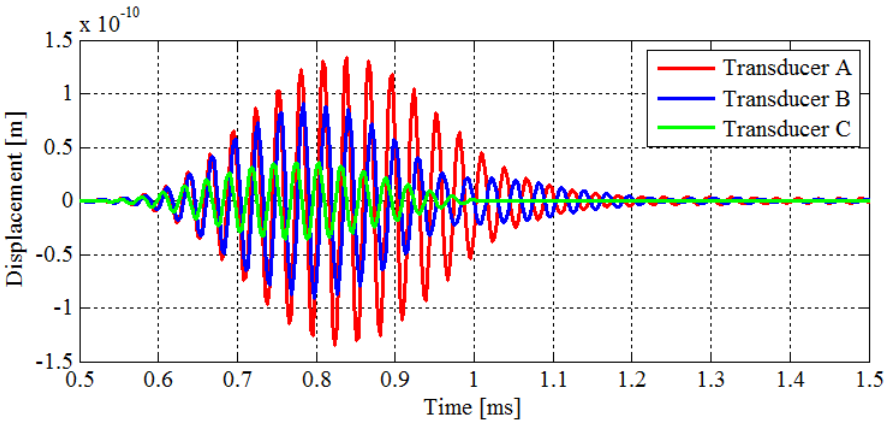

(c) Time history

Figure 4.2: The (a) modal amplitude, (b) frequency and (c) time response of the horizontal degree of freedom at the rail centre when excited by different transducer models

The objective of the design is to transfer the maximum energy possible into the web mode. If the web mode is strongly excited by a transducer, the peak amplitudes of the time history and the frequency response function will be large. An optimization criterion must be represented by a single value that will indicate whether a design is good or not depending on the objective statement. For a particular design, the optimization criterion can be taken as the area under the frequency response function. The frequency response

function is the best to be used for evaluating the optimization criterion as it is nicely smooth and continuous. Furthermore the area below the curve is well defined and can be easily used to clarify that the transducer operational frequency requirement has been satisfied.

The resultant of the area under the frequency response function is velocity. Velocity is an appropriate quantity to use as an optimization criterion an it is representative of the structure's kinetic energy. From the finite element method energy relations, kinetic energy is defined by:

$$E_k = \frac{1}{2}\dot{\mathbf{u}}^T \mathbf{M} \dot{\mathbf{u}} \tag{4.2}$$

where $\dot{\mathbf{u}}$ is the velocity of the structure and $\mathbf{M}$ is the mass matrix. Equation 4.2 shows that the square of velocity is directly proportional to energy. A high velocity measure of the web mode will therefore practically mean that a large amount of energy was put into the web mode.

The main interest for the design is to maximize the energy of the web mode only. Therefore, the area under the frequency response function of the web mode is representative of the energy in the web mode at the required operational frequency of the transducer. This makes the area under the windowed frequency response function a suitable optimization criterion for our transducer design.

Step 5: Formulation of constraints The bound constraints of the three design variables were determined in order to define the design space. The design space was defined based on the following factors which are controlled by the cost of materials and the transducer housing to be used:

- The diameter of the back mass should not be smaller than the diameter of the piezoelectric stack.
- The diameter of the back mass should allow room for electrical connectors within the housing.
- The overall length of the transducer should not be longer than the length of the housing.

The bound constraints are therefore as follows:

$$4\,mm \geq FM\ thickness \geq 10\,mm,$$

$$4\,mm \geq BM\ thickness \geq 10\,mm\ and$$

$$12.05\,mm \geq BM\ diameter \geq 15.5\,mm.$$

The transducer design problem is now well and completely formulated. In the next section we start off by analysing the nature of the problem, and then select an optimization method suitable for the problem.

4.1.2 Selection of the optimization method

From the transducer design optimization problem formulation discussed in section 4.1.1, the following points can be made about the nature of the problem:

- The dimensionality of the problem is low. There are only three design variables.
- The problem is of a practical nature. The SAFE3D method can be used to accurately predict the system response to various design variables. However, the SAFE3D model is computationally costly, therefore conducting a large number of evaluations can be costly.
- Depending on the optimization approach used, gradients may be required. The objective function depends implicitly on the design variables and the gradient of the objective function is not readily available. In addition, it needs to be repeated should the optimization criterion change. Alternatively, the gradients can be computed numerically using finite differences, which may increase the number of evaluations significantly.

At this point, no information is known about the nature of the optimization criterion (response surface) with regard to its continuity and smoothness on the design domain. To effectively use gradient based optimization methods, the objective function needs to be continuous and smooth. Should we conduct re-meshing of the transducer at any point of the optimization run, we run the risk of introducing numerical discontinuities due to abrupt changes in the discretization error. Considering the factors discussed thus far, it is clear that gradient based optimization methods on the actual function may not be suitable and practical for this problem. Non-smoothness and discontinuities can be handled by evolutionary approaches such as particle swarm optimization but that will drastically increase the computational cost of the problem in addition to running the risk of not having properly converged solutions.

Arora [3] suggest that to solve practical optimization problems, it is useful to develop a simplified function for the system that is explicitly related to the design variables. Such an explicit function is referred to as a meta-model. That is, it is a computationally

efficient model that approximates the computationally expensive original model. Meta-models can be generated using a method known as the response surface method. The first step in the response surface method involves conducting experimental observations by evaluating the original model at a number of selected sample points. This is referred to as Design of Experiments (DoE).

DoE involves evaluating the behaviour of a system by constructing a carefully selected set of experiments distributed over the design space, with all the input design parameters varied simultaneously. DoE has a number of advantages making the response surface method reliable:

- **High level of Control of variables**. The experimental sampling points are carefully selected.
- **Compatible with problems below 100 dimensions**. The method is useful and efficient in multidimensional parameter spaces.
- **Effortless collection of data**. Data can be collected via independent computer runs at a number of selected input settings (model's internal parameters, initial conditions and boundary conditions).
- **Controllable computational cost**. Once the experiment is set up, the evaluation process can be automated. Multiple computing resources can be used in parallel to conduct the experiment, thus making it computationally feasible to sample the design space densely.
- **Informative output data**. The output experimental data may help to clearly understand the model behaviour, provide clarity on what is a good design, and also help to make thorough decisions. Available methodologies can be used to analyse the collected experimental data in an effective way.

After experimental design, the final step in the response surface method is the approximation of the meta-model explaining the design problem. The response surface of the meta-model is constructed by interpolating a special function through experimental data. According to Fasshauer [11], a convenient and common approach to solving a scattered data interpolation problem is to assume that the interpolant is a linear combination of certain radially symmetric non-linear basis functions that are centred around each of the experimental data sites. This is referred to as Radial Basis Function (RBF) interpolation.

Once the response surface of the meta-model has been constructed, it is used in place of the original model in the optimization process. The process steps that will be adopted in this study to optimize a transducer design are summarised in Figure 4.3.

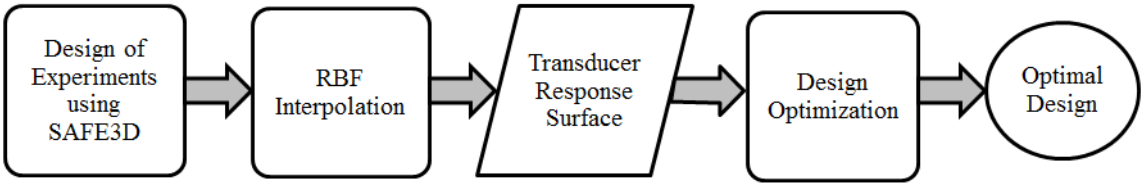

Figure 4.3: Process steps to optimize a transducer design using the Response Surface Method

4.2 Response Surface Method

4.2.1 Design of Experiments

The first step in DoE is to specify the factors (variables) influencing the experiment in which we simulate the performance of transducers within specified ranges. Thereafter, a set of transducer designs to be simulated within the specified ranges of the design variables need to be carefully selected. When conducting investigations, it is not viable to collect data for the entire sampling frame. As a general rule, it is known that the larger the sample size of simulated transducers the better we can approximate the transducer responses of transducers not in the samples that were simulated. However, each simulated response is time consuming and the fewer samples we use the faster we can start the optimization. As a result, a subset of data from the sampling frame that is representative of the entire design domain need to be carefully and systematically collected. The better the sampling the less points are required to accurately capture the characteristics of the system.

One way to select a set of random transducer designs that are appropriately distributed is to use the Latin Hypercube sampling (LHS) method over the defined ranges of the design variables. In their respective studies, Yin et.al [34], Janssen [15] and Saliby and Pacheco [30] recommended the use of the LHS method by demonstrating the superiority of the method over the widely used Monte Carlo sampling method. According to these sources, the Monte Carlo sampling method has a low sampling efficiency and needs a large number of sampling points. On the other hand, the LHS method has a better sampling efficiency and can render the same accuracy with less sampling points.

The LHS method involves a full stratification of the sampled distribution, with a random selection inside each stratum [30]. To sample an $s - dimensional$ space with N data points, the sampling space is divided into a series of strata by dividing the range of each variable into N equally sized intervals. The N sampling points are then randomly distributed over the sampling frame such that each stratum contains only one data point.

An example of a 2-dimensional LHS space sampled with 5 data points is illustrated in Figure 4.4. The variables are treated independently and each row/column is randomly sampled with one point only. The Matlab built-in function, `lhsdesign.m`, was used in this study to generate an LHS space.

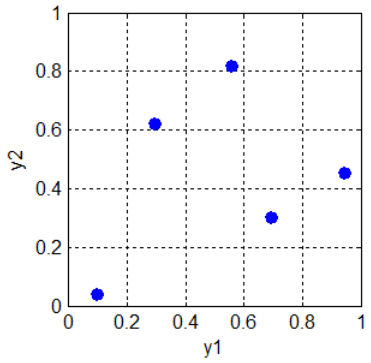

Figure 4.4: LHS sampled space with N=5

After identifying which transducer designs to simulate, each one needed to be simulated using SAFE3D to obtain their respective performances. This completes the computing of the simulated data. The data can now be used to construct a response surface that allows us to approximate the performance of transducers of which the performance is not known.

4.2.2 Construction of the Response Surface using Radial Basis Functions

Given a finite set of randomly scattered transducer designs and corresponding transducer performances (objective function values), we want to find a function $\tilde{f}$ (meta-model) that is an accurate representation of the simulated performances (original model). This will allow us to predict the response of designs other than the sampled designs. For this study, we consider interpolation meta-models. This is the meta-model that exactly matches the simulated performances for the transducer designs from the DoE. Mathematically, as stated in [11], the formulation for the response surface method is defined as :

Given a sample of data $(\mathbf{x}_j, f(\mathbf{x}_j))$, $j = 1, ..., N$, *with* $\mathbf{x}_j \in \mathbb{R}^s$, *find a (continuous) function* $\tilde{f}(\mathbf{x})$ *such that* $\tilde{f}(\mathbf{x}_j) = f(\mathbf{x}_i)$ *for* $j = 1, ..., N$.

$\mathbf{x}$ is the design vector that defines each transducer and f is a function representing the original model i.e. the simulated transducer performance. In this case $s = 3$ since

we have 3 design variables and N denotes the number of data points in the DoE sample. We choose the RBF response surface for our meta-model $\tilde{f}$ using a LHS sampled DoE.

The RBF method is a numerical analysis technique widely used for multivariate function interpolation. RBFs are used in a number of applications such as in the numerical solution of partial differential equations, data mining, machine learning and Kriging methods in statistics [24]. They have a capability to handle randomly distributed data points with improved consistency as compared to previous methods [24].

The RBF response surface $\tilde{f}$ is approximated by a linear combination of non-linear basis functions that are chosen. The basis functions are radially symmetric about their respective centre points hence appropriate scaling of the data is important. The interpolant function for the meta-model is constructed as:

$$\tilde{f}(\mathbf{x}) = \sum_{j=1}^{N} c_j \varphi \left(\| \mathbf{x} - \mathbf{x}_j \| \right), \tag{4.3}$$

where c_j are the coefficients of interpolation, φ is the basis function and the points $\mathbf{x}_j$ are the DoE transducer design points that are also chosen as the centre for each basis function.. The coefficients of interpolation are computed by requiring interpolation at the DoE sample points $\tilde{f}(\mathbf{x}_j) = f(\mathbf{x}_j)$, and given by:

$$\mathbf{c} = \mathbf{A}^{-1}\mathbf{f}, \tag{4.4}$$

with $\mathbf{A}$ defined as:

$$\mathbf{A}_{ij} = \varphi \left(\| \mathbf{x}_i - \mathbf{x}_j \| \right). \tag{4.5}$$

Some common radial basis functions used includes the Gaussian, multi-quadric, inverse multi-quadric and the Matern RBFs. In this study we choose the Gaussian RBF for it's smoothness. Smooth basis functions are ideal for the constructing of smooth functions to be used in optimization, as it makes more optimization strategies available to choose from. The Gaussian basis function is given by:

$$\varphi \left(\mathbf{x} \right) = e^{-(\epsilon \|\mathbf{x}\|)^2}. \tag{4.6}$$

Radial basis functions are characterized by a scalar parameter ϵ, known as the shape parameter. The shape parameter greatly influences the shape of the basis function. A higher shape parameter results in a spatially compact RBF, where the influence of ϵ is localized [11]. As $\epsilon \to 0$, the basis function spatial support becomes wider. The influence of the shape parameter on the basis function is demonstrated in Figure 4.5.

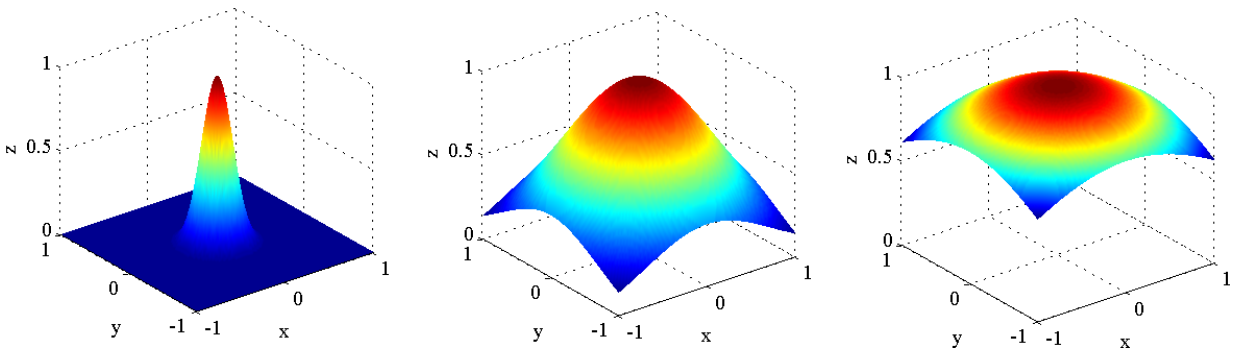

(a) $\epsilon = 5$ **(b)** $\epsilon = 1$ **(c)** $\epsilon = 0.5$

Figure 4.5: The influence of the shape parameter on the basis function

The shape parameter plays a significant role in RBF interpolation as it controls the accuracy and numerical stability of the interpolant function. It is therefore important to carefully choose an appropriate shape parameter. A strategy known as leave-one-out cross validation (LOOCV) is often used to compute the RBF shape parameter [28]. In the LOOCV method, the given N data points are split into two sets. The first set consisting of $N-1$ data points is used to construct the interpolant while predicting the point in the second set (the remaining data point) used to compute an error for the interpolation. This procedure is repeated for all combinations of leaving out a point i.e. N times. The LOOCV error is then computed as the sum of errors squared:

$$LOOCV(\epsilon) = \sum_{k=1}^{N} \mid \tilde{f}_k(\mathbf{x}_k) - f(\mathbf{x}_k) \mid^2 . \tag{4.7}$$

$\mathbf{x}_k$ is the validation point left out when computing the interpolant $\tilde{f}_k$. The computation of the LOOCV error using equation 4.7 is very expensive as the computational complexity is of order $O(N^4)$. To improve the computational cost, Rippa demonstrated in [28] that equation 4.7 can be simplified to:

$$LOOCV(\epsilon) = \sum_{k=1}^{N} \mid \frac{c_k}{A_{kk}^{-1}} \mid^2 . \tag{4.8}$$

The coefficients of interpolation c_k and the diagonal of the interpolation matrix A_{kk} are computed using the full data set. Once A is computed the complexity becomes N as the inverse of a diagonal matrix is $O(N)$.

4.2.3 The Response Surface for the Rail Web Transducer

4.2.3.1 DoE for Transducer Design

In RBF interpolation, the interpolant is usually associated with larger errors at and closer to the edges of the design space. This is because the density of points along an edge is lower than in the interior. To improve the accuracy of the response surface of the meta-model at the bounds of the design space, it was decided to perform the interpolation by also including transducer design points that lie outside the design space. A second larger domain, which we refer to as the sampling space, was selected. The sampling space is an enlarged design space that is used to improve the accuracy of the objective function at the bounds of the actual space. The sampling space was chosen as follows:

$$1.5 \geq x_1 \geq 12.5,$$

$$1.5 \geq x_2 \geq 12.5 \; and$$

$$12 \geq x_3 \geq 20.$$

Figure 4.6 is an illustration of the design space and the sampling space. The design space fits inside the sampling space. The BM diameter could not be reduced to less than $12mm$ because that would be less than the diameter of the stack, which would be undesirable.

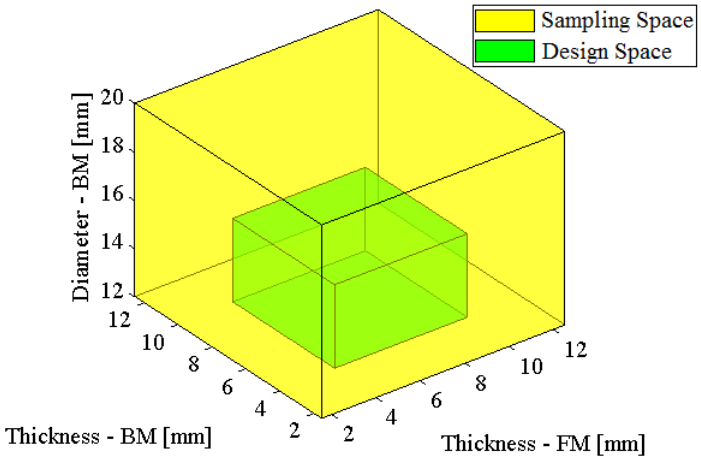

Figure 4.6: The design space and the sampling space

A good value of the shape parameter depends on the number and distribution of data points used for RBF interpolation [28]. To demonstrate the effect of the number of data

points N, three sets of data are considered. The sets respectively consist of 125, 250 and 500 Latin Hypercube sampled data points. The sampling procedure was carried out using a built-in function in Matlab called `lhsdesign.m`. Figure 4.7 shows the three sets of DoE data and their optimization criterion values computed using the SAFE3D method.

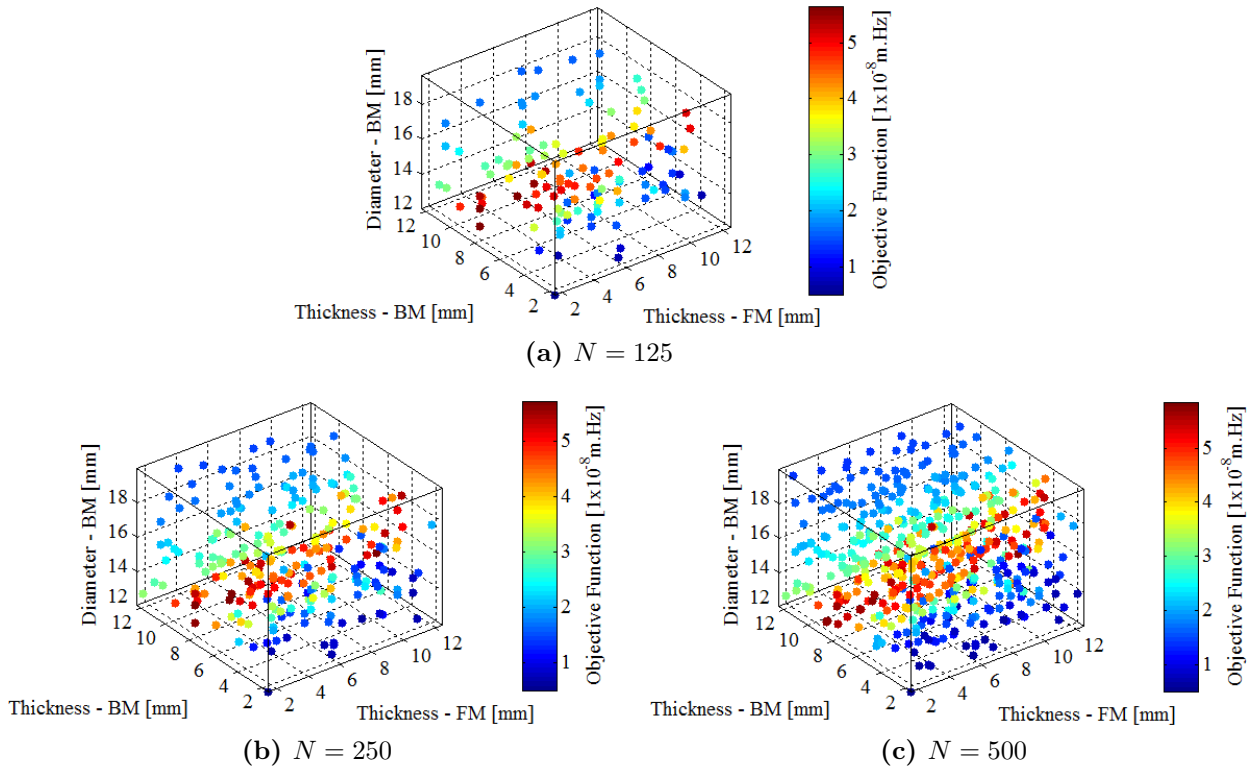

(a) $N = 125$

(b) $N = 250$

(c) $N = 500$

Figure 4.7: DoE transducer design points in the larger sampling space.

4.2.3.2 Minimization of the RBF shape parameter

The LOOCV error was computed by solving a 1D minimization problem of equation 4.8. The procedure was implemented in Matlab using a built-in function `fminbnd.m`.

The predicted shape parameter values and their corresponding LOOCV errors normalised with respect to the sample size N are reported in Table 4.2. It is evident that an increase in the number of data points lead to an increase in optimal shape parameter as expected, as the spatial support for a higher number of points can be more localized. The LOOCV error shows that using a large sample size will lead to the accuracy of the basis function improving.

Table 4.2: Shape parameters and associated error values for N number of data points in RBF interpolation

N	ϵ	$LOOCV/N$
125	3.4226	0.0133
250	7.0037	0.0086
500	9.8863	0.0024

Plotted in Figure 4.8 is the $LOOCV/N$ error as a function of the shape parameter. The results from Table 4.2 are also plotted on the figure using square markers. At lower values of epsilon the error is high due to numerical instability associated with an ill-conditioned A matrix. At higher values of epsilon the error increases as the basis function support is too local resulting in a response that reduces to zero away from the centre of the basis function. We chose the smallest epsilon that effectively minimised the LOOCV error. The minimum epsilon implies that we prefer the basis function with the widest spatial support, as it reduces the possibility of induced local minima in the meta model. The optimal shape parameters in Table 4.2 are clearly in agreement with Figure 4.8.

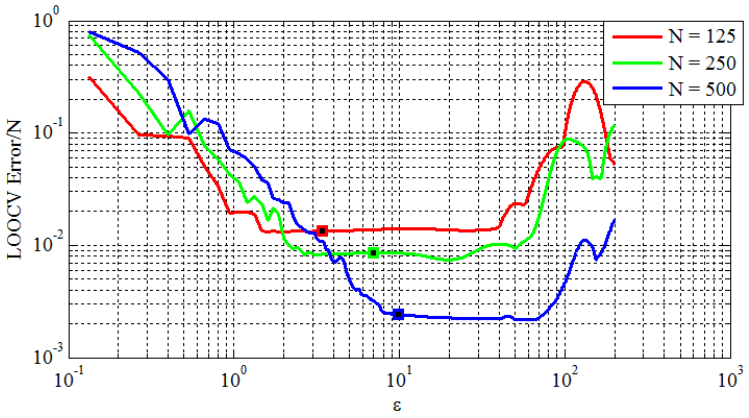

Figure 4.8: The LOOCV error as a function of the RBF shape parameter

4.2.3.3 The Transducer Design Response Surface

The response surface predicted by RBF interpolation using 500 data points is plotted in Figure 4.9. Within the design space, it was found that there are three categories of transducer designs; those with the modal amplitude peak of the web mode at a frequency of less than $35kHz$, greater than $35kHz$ and at or approximately at $35kHz$. As expected, designs with the web modal amplitude peak closer to $35kHz$ are associated with high function values, thereby indicating good performance at $35kHz$.

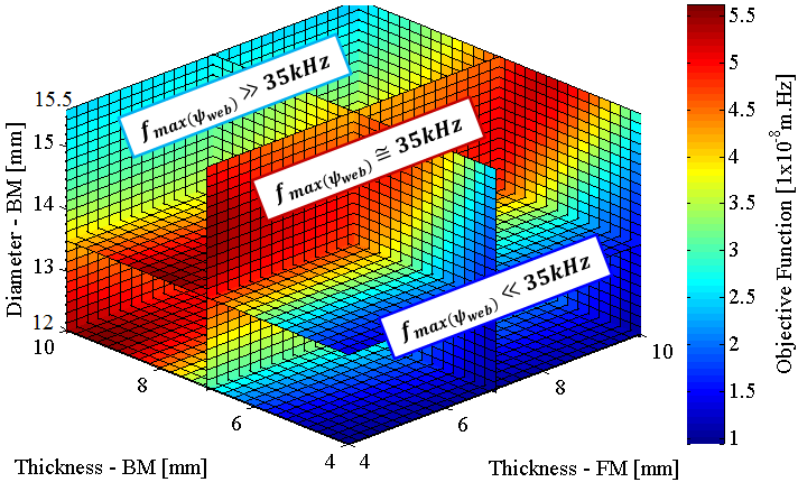

Figure 4.9: The predicted objective function

To get a clear visualization of the response surface, we look at the slice plots of the function at different FM thicknesses in Figure 4.10. It is clearly illustrated from the slice plots that the response surface contain more than one local maximum. The response surface has high values at the boundary where $t_{FM} = 4mm$. Moving from this boundary, we see that the function values decreases until a front mass thickness of approximately $8mm$ is reached, and then start to increase as we move towards $10mm$.

4.2.3.4 Validation of the predicted response surface

To evaluate the accuracy of the response surface values predicted by RBF interpolation, 27 design points arranged in the form of a grid over the sampling space were selected for error analysis. The RBF predicted function values were compared to the function values computed from the SAFE3D method. The error percentage associated with the selected points are plotted in Figure 4.11 for the three data sets.

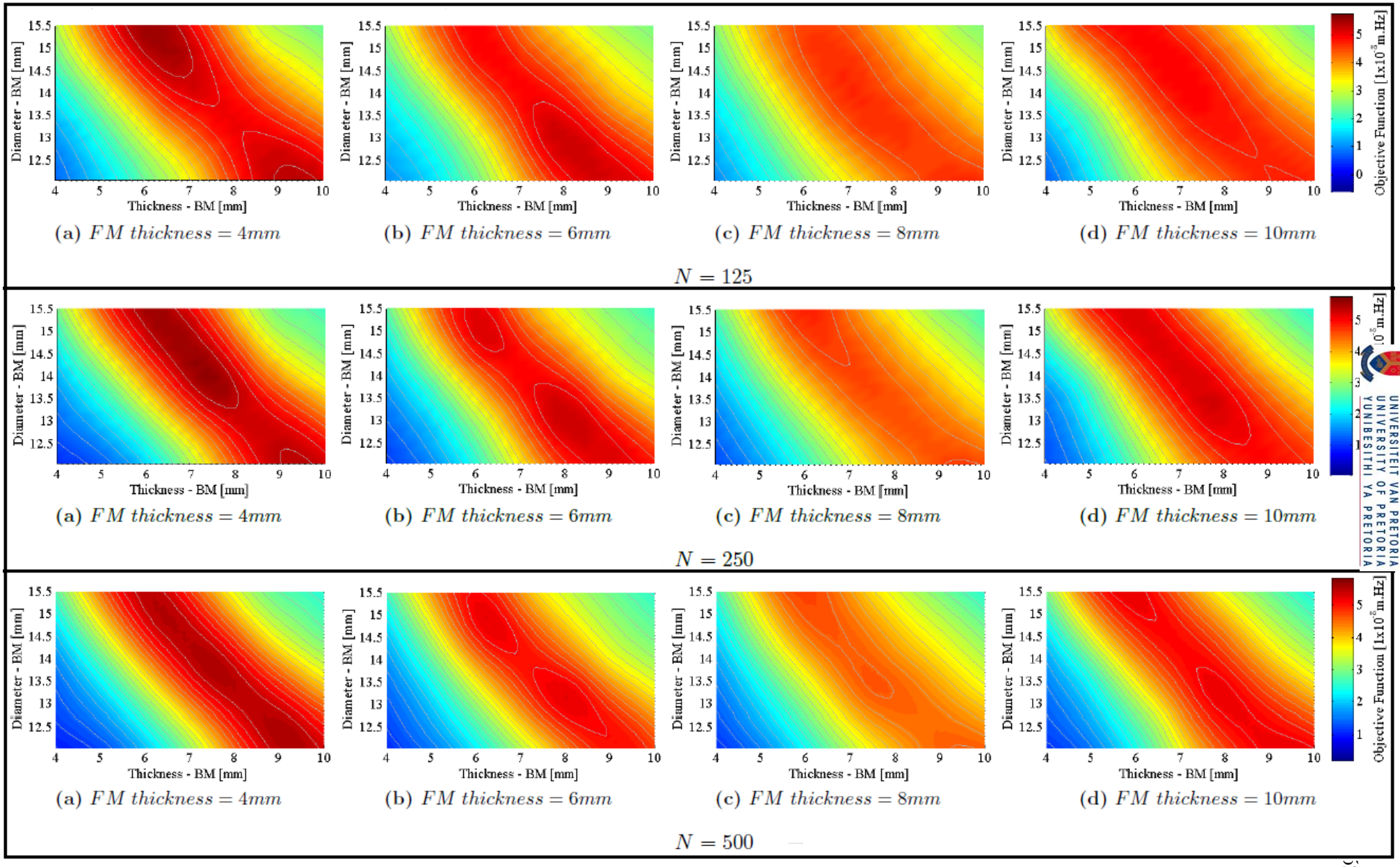

Figure 4.10: Slice plots of the approximated transducer response surface at different front mass thicknesses for $N = 125$, $N250$ and $N = 500$

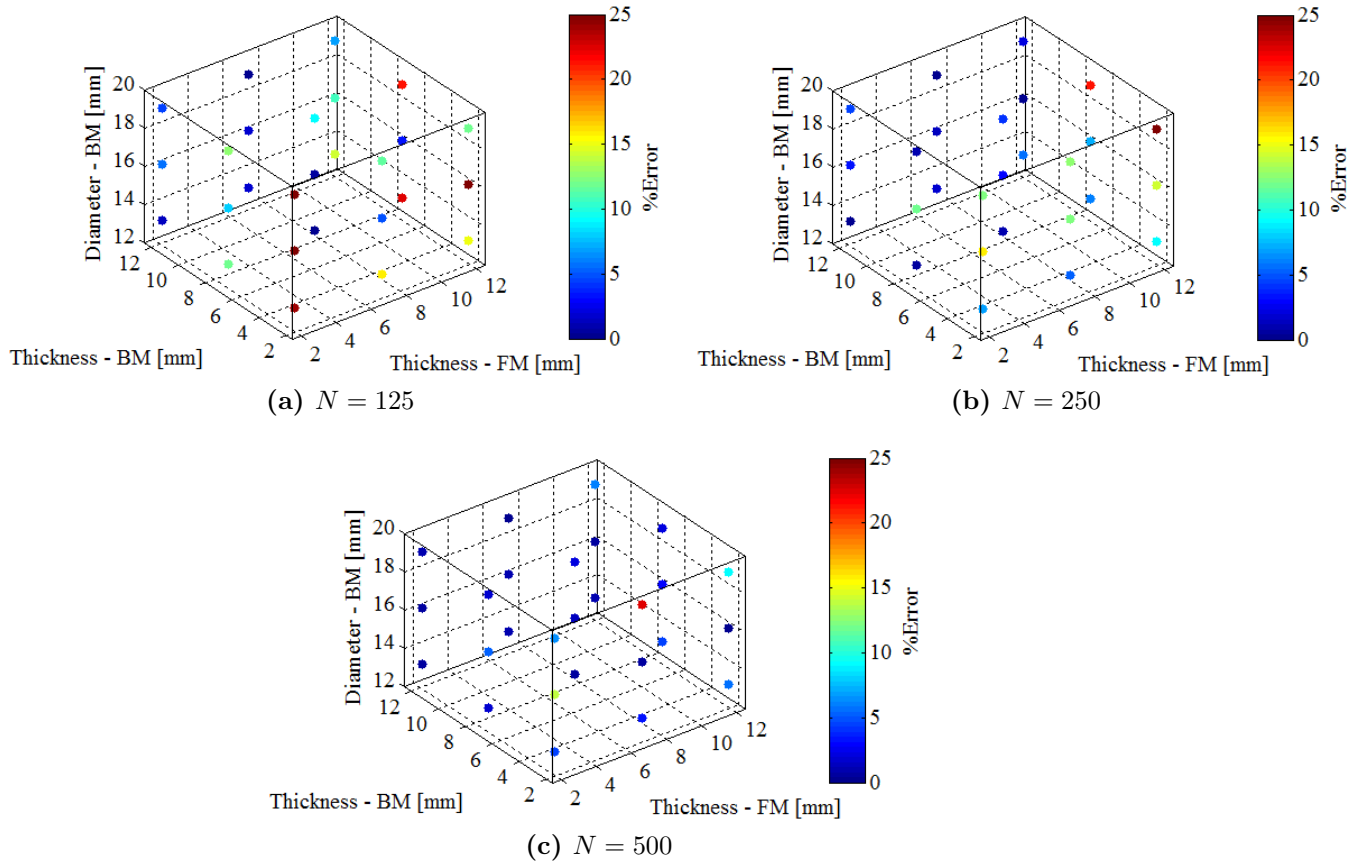

(a) $N = 125$ **(b)** $N = 250$

(c) $N = 500$

Figure 4.11: The errors associated with the approximated response surface for different values of N in the sampling space

It is seen from Figure 4.11 that the errors are high at the boundary of the sampling space as compared to the interior. As expected the approximation errors decreases as more data points are used in the response surface, thus improving the quality of the RBF response surface.

Now to demonstrate the significance of using a sampling space to approximate the response surface, we evaluate the accuracy of a number of points that are within the design space. Figure 4.12 shows the errors associated with the design space. The errors within the design space are significantly smaller as compared to those within the sampling space.

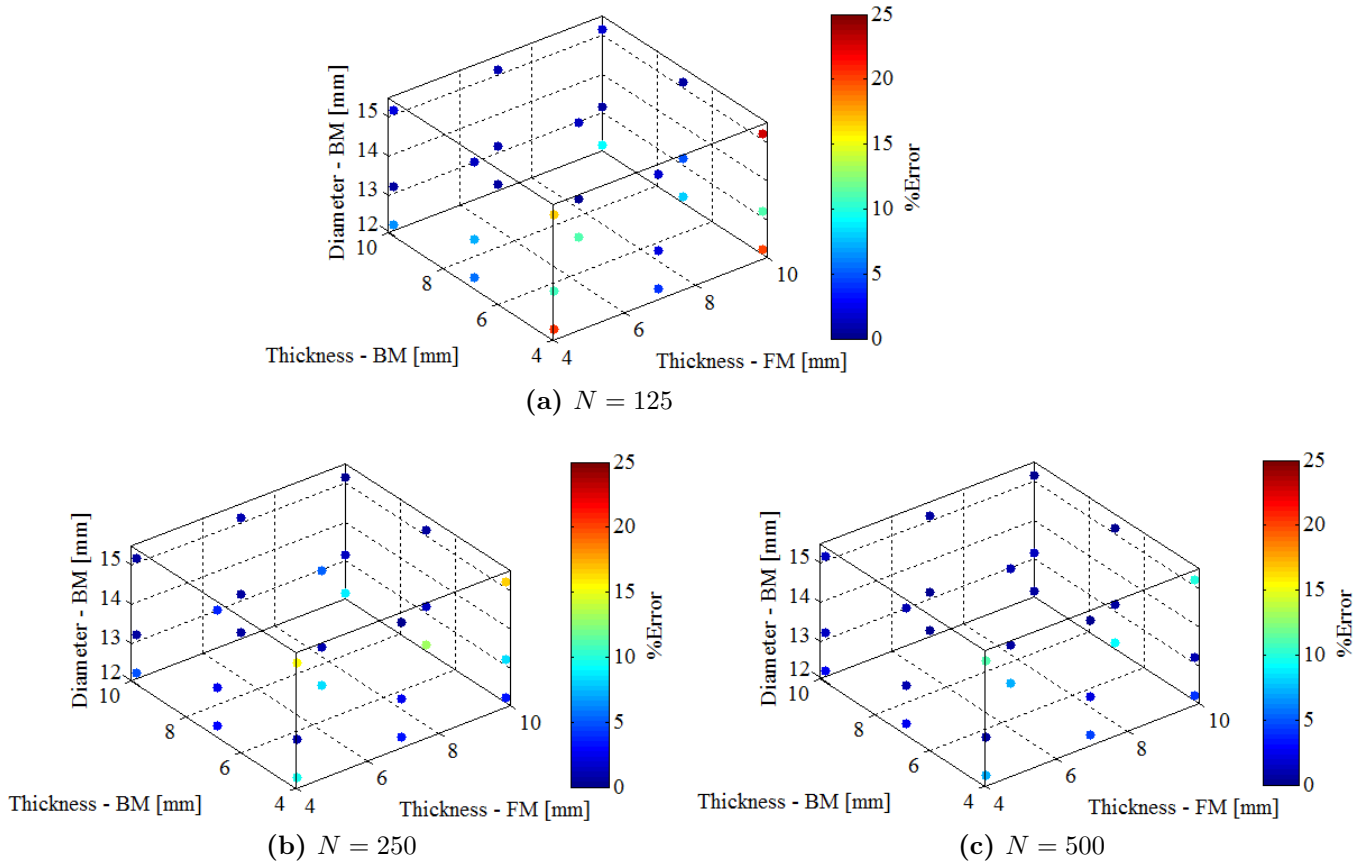

(a) $N = 125$

(b) $N = 250$

(c) $N = 500$

Figure 4.12: The errors associated with the approximated response surface for different values of N in the design space

The response surface predicting the performance of transducer designs has been successfully constructed. We are now ready to proceed with the optimization of the design. In design optimization, we refer to the approximated response surface of the meta model as the objective function for the design problem.

4.3 The Mathematical Design Optimization Model

Following the optimization formulation for the design of the rail web transducer in Section 4.1.1, the standard mathematical design optimization model is stated as follows:

Find a vector $\mathbf{x} = \{x_1, x_2, x_3\}^T$ of design variables to

Maximize the response of the rail web mode to piezoelectric transducer excitation given by the objective function:

$$f(\mathbf{x}) = A(\mathbf{x}), \tag{4.9}$$

subject to three inequality constraints:

$$4 \leq x_1 \leq 10,$$

$$4 \leq x_2 \leq 10 \; and$$

$$12.05 \leq x_3 \leq 15.5$$

with the design variables defined as:

$$x_1 - FM\ thickness$$

$$x_2 - BM\ thickness$$

$$x_3 - BM\ diameter$$

The function f is the design objective function approximated using the response surface. It denotes the energy transferred into the rail web mode by the piezoelectric transducer.

The derivative-free Nelder-Mead minimizer was used. This optimizer is implemented in `fminsearch` and is designed for multidimensional unconstrained non-linear minimization problems. The constrained optimization problem presented is transformed to an unconstrained problem by using the exterior penalty method to handle the constraints. In the exterior penalty method, the unconstrained optimization problem is formed by adding a penalty function to the objective function for each violated constraint. The penalty function with appropriate penalty parameter enforces the searching algorithm to remain feasible.

The unconstrained minimization problem for the Nelder-Mead minimizer is stated as:
Find a vector $\mathbf{x} = \{x_1, x_2, x_3\}^T$ of design variables to
Minimize the function:

$$\Phi(\mathbf{x}) = -f(\mathbf{x}) + p_1 \sum_{x_i<LB} (x_i - LB_i)^2 + p_2 \sum_{x_i>UB} (x_i - UB_i)^2 \tag{4.10}$$

where $p_1\ and\ p_2$ are the penalty parameters for a design variable x_i violating its lower bound constraint LB_i and its upper bound constraint UB_i, respectively. Note that the objective function is now multiplied by a negative sign since we are now dealing with a minimization problem. We will refer to the problem as a maximization problem although the minimization formulated problem is solved due to available optimization algorithms.

4.4 Optimization of the Transducer Design Objective Function

4.4.1 The local optimum designs and the global optimum transducer design

In this section we discuss the designs associated with an optimum performance as predicted by the optimization algorithm. In optimum design, it is not always the case that the design will converge to the global maximum when there exist more than one local maxima. Convergence is usually driven towards one of the local maxima, depending on the starting point of the algorithm. To capture all the local maxima in the objective function, the optimization procedure was carried out 100 times with the starting points randomly selected within the design space. Plotted in Figure 4.13 is a histogram of the local optimum designs predicted from the 100 runs. Each bin in the histogram represents the cost function value of a local optimal transducer, with the height of the bin indicating the number of times that the optimizer converged to a local optimum with that function value out of the 100 runs. The three sets of data points in RBF interpolation were all considered for comparison.

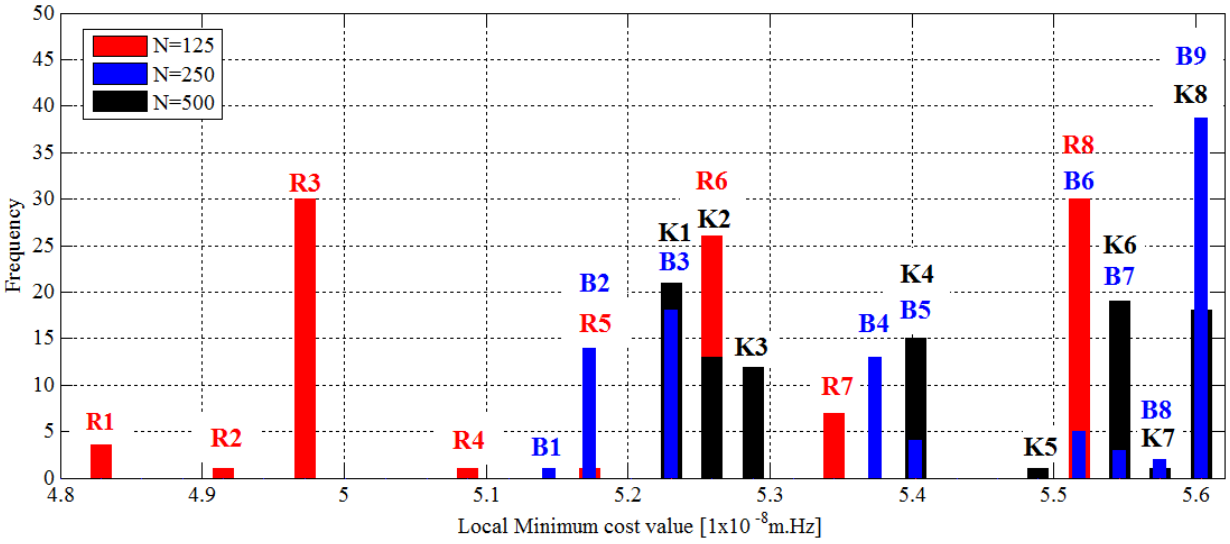

Figure 4.13: The local optimum designs

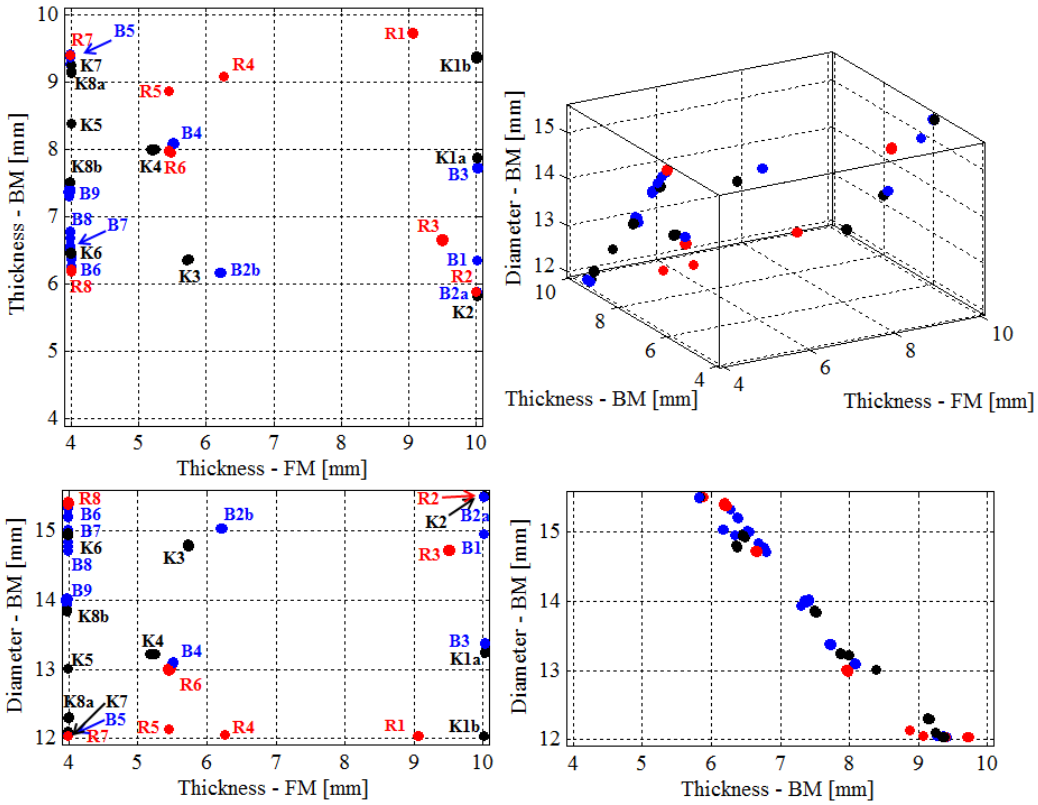

Figure 4.14: Local maximum designs

In Figure 4.14, the locations of the local optima are shown within the design space. After careful consideration of Figures 4.13 and 4.14, the following observations need can be made:

- For N=125, the function values of the local maxima ranges between 4.8-5.52. For N=250 and N=500, we notice a similar trend of the local maximum function values. They are all located more to the right of the histogram.

- For the three sets of data, N = 125, N = 250 and N = 500; a total of 8, 9 and 8 local maxima were respectively computed. Most of the local maxima found for N=500, were also predicted for either N=125 or N=250.

- A single bin in the histogram may contain different transducer designs, for example, bins K1, K8 and B2 respectively contain designs K1a and K1b, K8a and K8b and B2a and B2b. A similar characteristic between different designs of the same bin is the value of the objective function, implying that they have a similar performance. For bins K1 and K8, it is observed that the designs have the same FM thickness and the same size of the BM. On the other hand, for the designs in bin B2, the thickness of the FM is different, and the dimensions of the BM seem to be close.

- As reflected by the slice plots of the objective function in Figure 4.10, Figure 4.14 also suggest that there is an area of low performance at approximately $t_{FM} = 8mm$. Most of the predicted optimum designs are clustered at the boundaries of the FM thickness, where the transducer designs are characterised by good performance.
- There exist a threshold on the BM thickness that an optimum design can have.
- The histogram indicates that there exist a global maximum with a function value of $5.6e-8mHz$, that was predicted in bins B9 and K8. It can be seen in Figure 4.14 that the designs B9 and K8b are the same, however due to computational errors, the two predictions are slightly different.

For the three sets of data, the results for N=500 are more trusted as it was demonstrated earlier in this section that the associated errors are lower. In Figure 4.15, the local optimum designs are plotted on the slice plots of the objective function, with the K designs labelled. It is seen that the local maxima found by the optimization algorithm are in good agreement with the local maxima of the objective function.

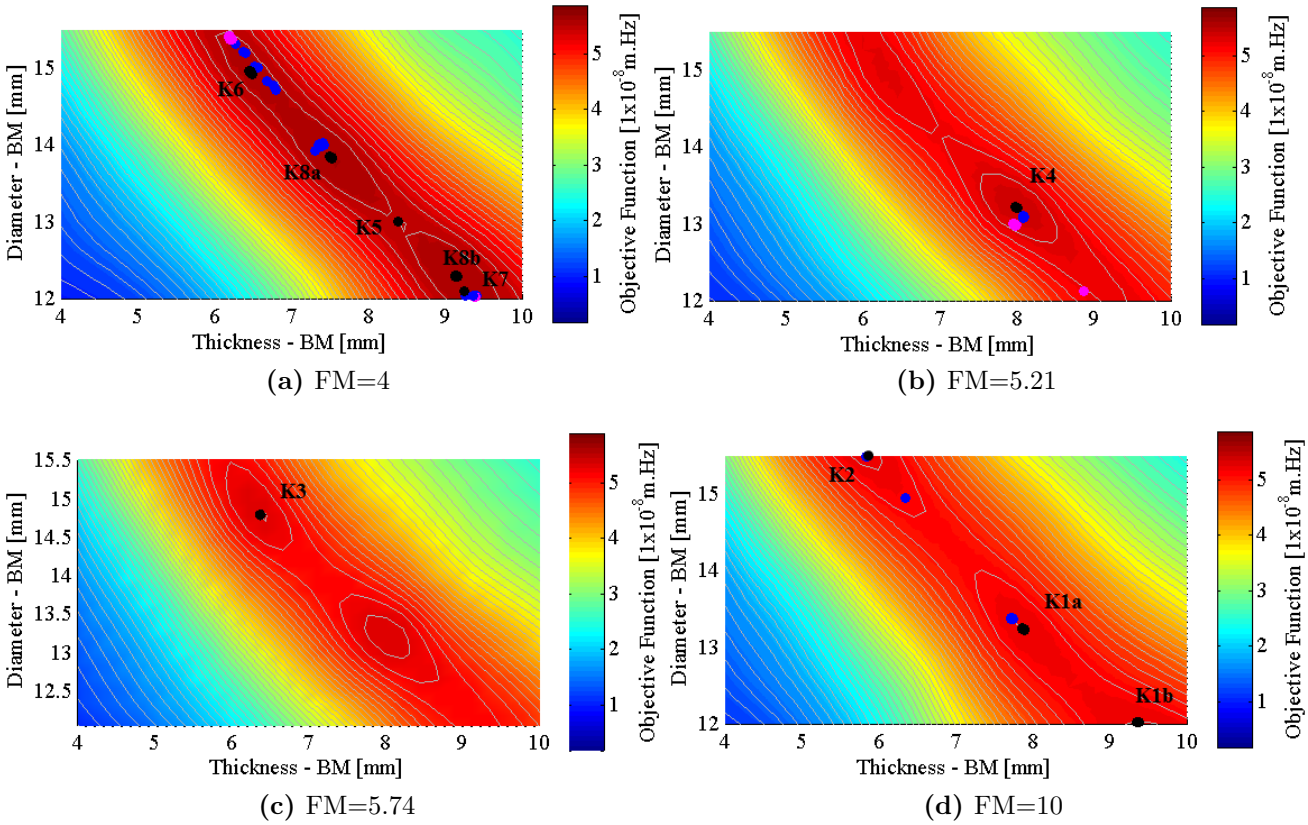

(a) FM=4 **(b)** FM=5.21

(c) FM=5.74 **(d)** FM=10

Figure 4.15: The location of the local optimum designs at FM thicknesses associated with the K designs

4.4.2 Validation of the global optimum design

It was found from section 4.4.1 that there exist two global optimum designs; the K8a and K8b designs, shown in Figure 4.16. RBF interpolation predicted that the performance value associated with the two designs is approximately $5.6e-8mHz$. To verify the accuracy of this prediction, the SAFE3D method was used. The results from RBF interpolation and the SAFE3D method are compared in Table 4.3.

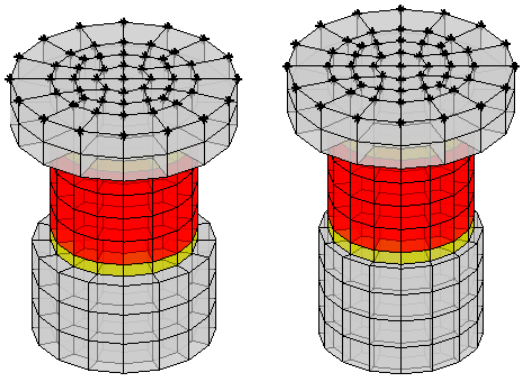

(a) Design K8a **(b)** Design K8b

Figure 4.16: The two best transducer designs found.

	Design K8a	Design K8b
FM thickness	4	4
BM thickness	7.6	9.1
BM diameter	13.8	12.3
RBF predicted performance	5.6114	5.6013
SAFE3D predicted performance	5.5968	5.5712
$\|\%Error\|$	0.261	0.5403

Table 4.3: The global optimum designs.

It is evident from the table that the agreement between the RBF method and the SAFE3D method is exceptionally good. The error percentage show that the prediction for the K8a design was more accurate than that of the K8b design. The frequency response functions and deformation plots at $35kHz$ for the two designs are compared in Figures 4.17 and 4.18.

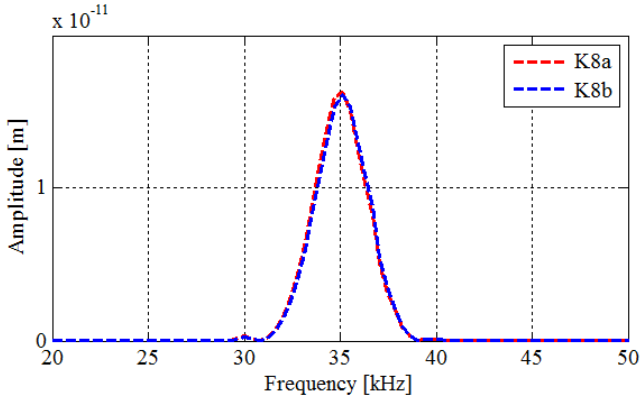

Figure 4.17: The frequency response functions of the two global optimum designs

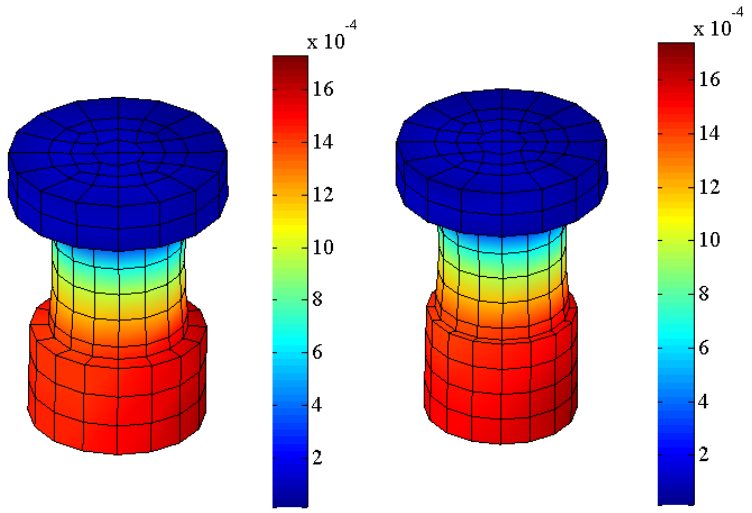

(a) K8a **(b)** K8b

Figure 4.18: Displacement deformation plots of the two best transducer designs.

The results show that although the two designs are different, their performance measures are almost equal and cannot be noticed. The K8a is selected as the best design as the correlation between the two predictions is very good.

4.4.3 Interpretation of results

From the previous discussion, it was shown that there exist two different designs with the same performance measure. Table 4.3 showed that the two designs have the same FM dimensions but different BM dimensions. By further evaluating the geometrical parameters of the two designs, it is found that the mass of their back masses are very close.

The back mass of K8a design is $8.866\times10^{-3}kg$ while for the K8b design it is $8.434\times10^{-3}kg$. In Figure 4.19, constant back mass designs are evaluated for different geometrical designs in the design space. It is evident that the constant mass contours matches those associated with the response surface of the design problem. It is therefore concluded that the mass of the back mass greatly influences the performance of a transducer. For the problem in this study, a transducer performs very well if the back mass is approximately $8.5\times10^{-3}kg$.

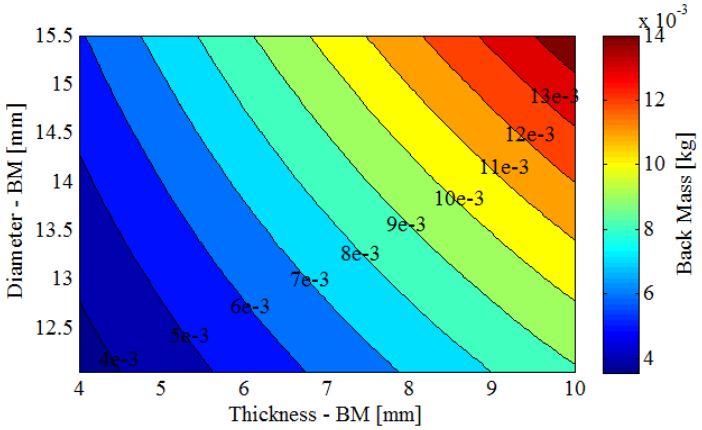

Figure 4.19: Transducer designs with constant back mass contours

The response surface of the design problem (Section 4.3.2) suggested the performance of a design improves as a front mass thickness of $4mm$ was approached, hence our optimum design was found to lie on the boundary of the design space. Now an interesting finding is that if the flexibility of the problem was not constrained by the set FM thickness bound, a design with a better performance than K8a would be predicted by the optimization algorithm. The slice plots of the response surface in the vicinity of the K8a design in Figure 4.20 reveal that there exists a plenty of designs outside the design space that performs very well. In addition to the back mass, the front mass thickness is the second factor that greatly influences the design performance.

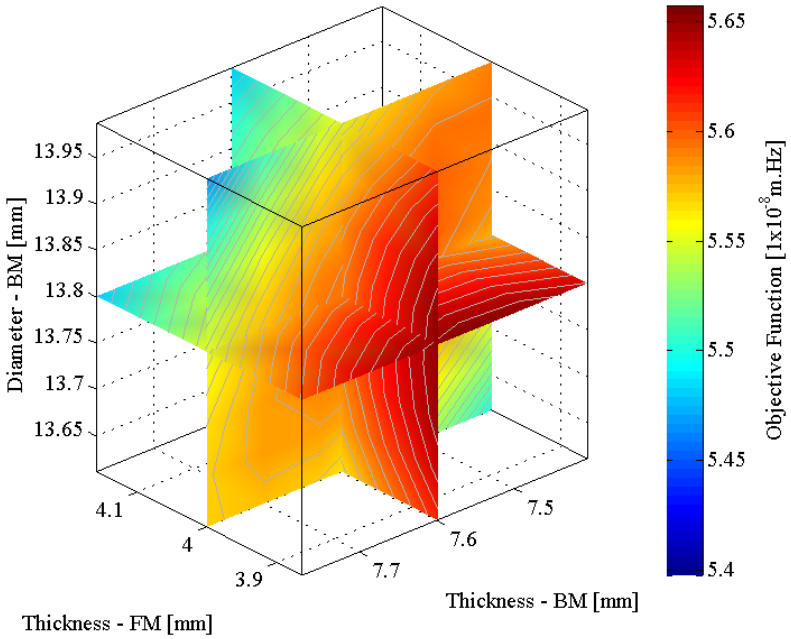

Figure 4.20: Slice plots of the response surface in the vicinity of the K8a design

In Figure 4.21 we evaluate the performance of six selected designs around the global optimum (K8a) obtained by increasing and decreasing each of the design variables independently. The geometrical parameters of the 6 perturbed transducer designs are tabulated in Table .

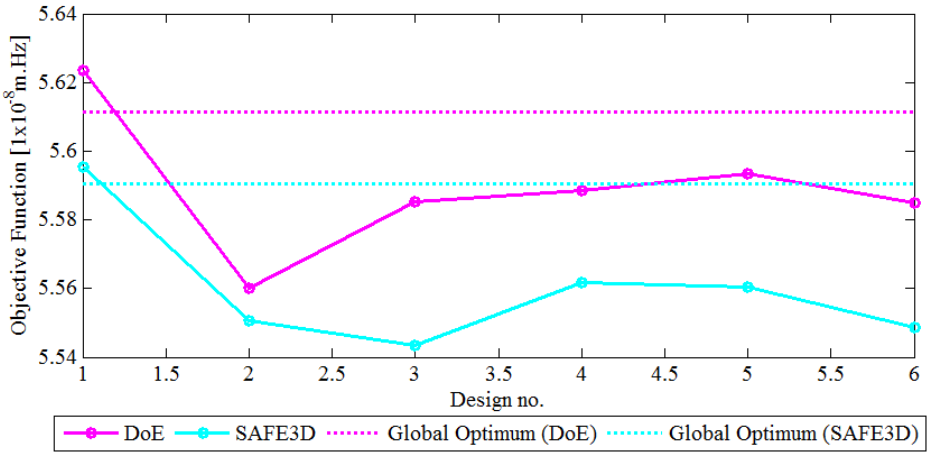

Figure 4.21: The performance of 6 selected designs around the K8a design

Design	t_{FM}	t_{BM}	d_{BM}	Parameter change
1	3.94	7.6	13.8	$\triangle t_{FM} = 60\mu m$
2	4.08	7.6	13.8	$\triangle t_{FM} = 80\mu m$
3	4.00	7.48	13.8	$\triangle t_{BM} = 120\mu m$
4	4.00	7.63	13.8	$\triangle t_{BM} = 30\mu m$
5	4.00	7.6	13.83	$\triangle d_{BM} = 30\mu m$
6	4.00	7.6	13.72	$\triangle d_{BM} = 80\mu m$

Table 4.4: Six transducer designs obtained by changing each of the design variables of the K8a design independently

The results show that the trend between SAFE3D predictions and the response surface method predictions is similar. The two approaches suggest that the only way to improve the design is to decrease the thickness of the front mass. The sensitivity of the design to a parameter change increase as the tolerance increases. It is found that when a parameter change is within $30\mu m$ the design is not too sensitive. A conclusion can be made from the results that manufacturing errors within $30\mu m$ are acceptable.

4.5 Conclusion on transducer design

In this Chapter, a design optimization study was carried out to design a piezoelectric transducer capable of exciting the rail web mode strongly when driven by a $35kHz$ centre frequency hanning-windowed tone-burst signal. The optimization process was carried out on the response surface of the meta-model approximated by first conducting a design of experiments using the SAFE3D modelling method and thereafter fitting RBF surfaces over the collected data. The accuracy of the meta model over the design space was validated using SAFE3D and the computational errors were found to be within an acceptable limit.

To search for a transducer design with an optimum performance, a gradient free optimization approach was followed, hence the response surface method was selected. Not only did the gradient free optimization approach simplify the computational complexity and cost, but it also helped to avoid possible function discontinuity issues. The optimization algorithm predicted that there exist two global optimum designs, K8a and K8b. The SAFE3D method justified that the response surface method predicted the performance of the two designs very well. The K8a design was selected as the best design as its percentage error was found to be the smallest.

This Chapter has demonstrated the usefulness of the response surface method when solving practical design optimization problems. The method was found to be efficient and reliable. Another notable aspect of optimizing using the response surface method is that it does not only output an optimum design but also provide concrete modelling results that can be converted to informative plots and used to attain a clear insight into the system being explored prior to optimization.

In the following chapter (Chapter 5), the optimum transducer design (K8a) is manufactured and experimental measurement is used to verify the accuracy of the transducer numerical model solved in SAFE3D.

CHAPTER 5

Manufacturing and Validation of the Optimum transducer design

A piezoelectric transducer capable of exciting the rail web mode optimally at a frequency of $35kHz$ has been designed in Chapter 4 using design optimization methods. Both the response surface and the SAFE3D methods predicted the same objective function value for the optimum design. In this Chapter, the optimum transducer design is manufactured and tested experimentally to validate the results presented by the response surface method and SAFE3D.

5.1 Manufacturing of the optimum transducer

The optimum transducer design was referred to as design K8a in Chapter 4 and its geometrical dimensions are tabulated in Table 4.3. The transducer uses a piezoelectric stack that is readily available at the CSIR, as stated in Chapter 4. The front and backing sections of the transducer are the only parts that need to be manufactured. A computer aided design software was used to produce detailed engineering drawings of the design in order to ensure clear communication with the manufacturing department at the CSIR.

In Figure 5.1, a computer aided design model of the actual transducer to be manufactured is shown with the SAFE3D model plotted alongside.

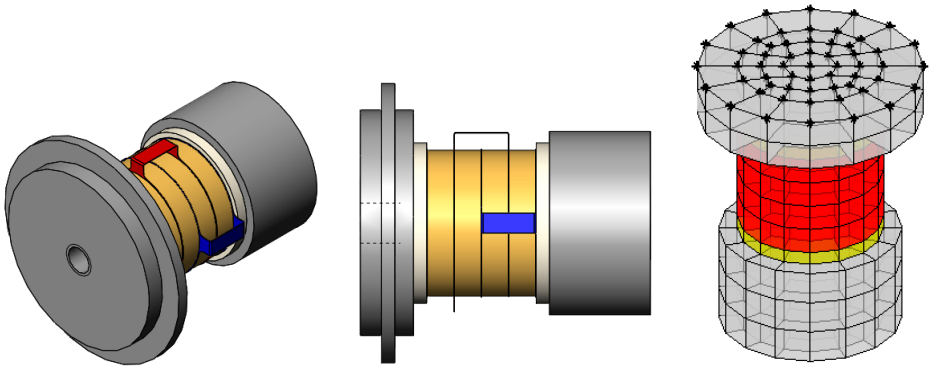

(a) Isometric view of the actual design for manufacturing

(b) Side view of the actual design for manufacturing

(c) SAFE3D model

Figure 5.1: The optimal transducer

Comparing the actual design for manufacturing and the SAFE3D model, it is clear that the two models have a number of differences. The following assumptions were made in the SAFE3D model:

- The effect of the bolt is negligible.
- The front and backing masses do not contain any holes drilled through.
- The electrical voltage can be applied to the interface nodes between piezoelectric disks, and therefore the brass electrodes need not be modelled.

The two important points worth noting regarding the actual transducer are as follows:

- A glue material was used to keep the piezoelectric ceramic stack with electrodes together.
- An external flange was added to the front mass. The flange serves the purpose of supporting the transducer when put in the housing.

The detail design of the front mass was controlled more by the transducer housing. Note that the transducer housing is not presented in this work as it is not part of the scope. The front mass was manufactured by machining a workpiece to the required profile using a turning process. A hole was then drilled and threaded at the centre to fit an $M3$ bolt.

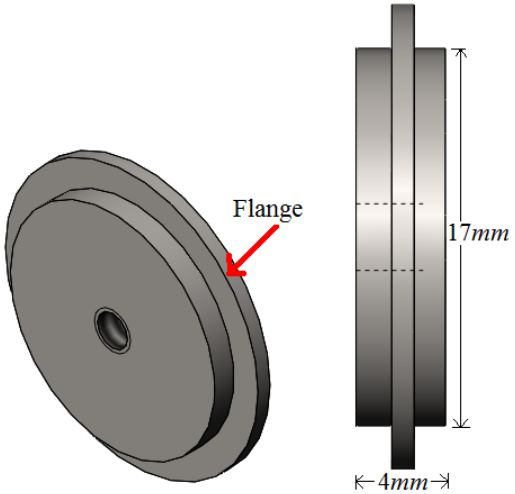

(a) Isometric view **(b)** Side view

Figure 5.2: The front mass of the optimum transducer design

The back mass of the transducer was also machined using a turning process. A hole was drilled and countersunk at the centre to allow for the bolt to remain flush with the back mass surface.

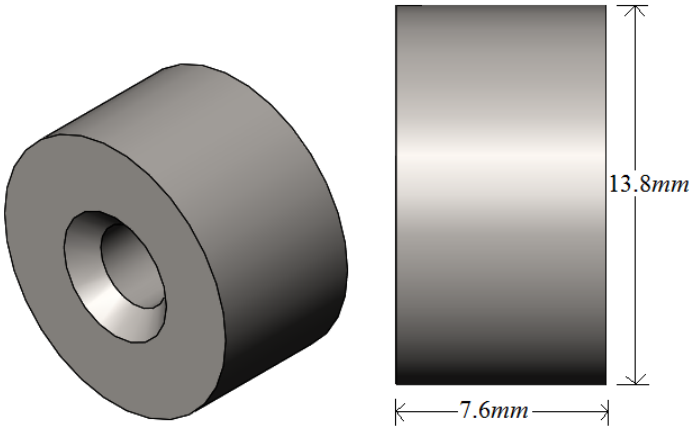

(a) Isometric view **(b)** Side view

Figure 5.3: The back mass of the optimum transducer design

After the manufacturing of the required components, the components were sent to the relevant sub-unit at the CSIR to assemble the transducer. Two brass electrodes were used in the electrical unit to allow for electrical connection when driving the transducer system. Each of the electrodes connect surfaces (on the piezoelectric ceramic) of the same potential. One electrode serves as the reference or ground. The connection of the electrical unit is shown in detail in Figure 5.4.

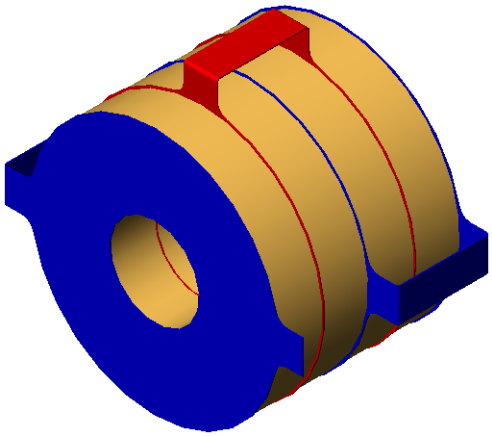

Figure 5.4: The connection of the brass electrodes to the piezoelectric ceramic disks

5.2 Transducer Resonance and Anti-resonance Test

After assembling the transducer system, the procedure that followed was to evaluate the resonance and anti-resonance frequencies of the longitudinal mode. The resonance and anti-resonance frequencies are computed by imposing appropriate boundary conditions on the system. The resonance frequency is obtained under short circuit conditions, where the voltage drop between the electrodes is set to zero, and the antiresonance frequencies are obtained under open circuit conditions where the voltage drop is non-zero. A deformation plot of the transducer under resonance frequency conditions is plotted in Figure 5.5, and in table 5.1 the results obtained from the experimental test and the 3D FEM MATLAB model are compared.

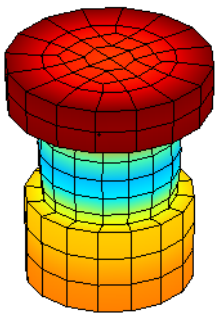

Figure 5.5: Transducer under resonance frequency conditions

It is clear that the transducer is in the longitudinal deformation mode as expected. Under anti-resonance frequency conditions, the deformation mode is also found to be longitudinal but at a different frequency.

	Resonance frequency, $[kHz]$	Anti-resonance frequency, $[kHz]$
Test measurement	51.0	60.0
3D FEM	55.953	62.429

Table 5.1: The resonance and anti-resonance frequencies of the optimum transducer

Table 5.1 shows that the two approaches predicted different results. The frequencies predicted by 3D FEM are higher compared to those obtained from the test measurement. This deviation is believed to be due to the differences in the manufactured transducer and the 3D model. The computed frequencies from 3D FEM are not fully trusted.

5.3 Validation of the optimum design using experimental measurement

To help make a concrete conclusion regarding the manufactured transducer, an experimental measurement evaluating the response of the guided waves propagating though the rail track when excited by the transducer was performed.

The experimental measurement for the optimal transducer was conducted in the same manner used for the experimental measurement of the old transducer in Section 3.4.

The experimental results are compared to SAFE3D results in Figure 5.6.

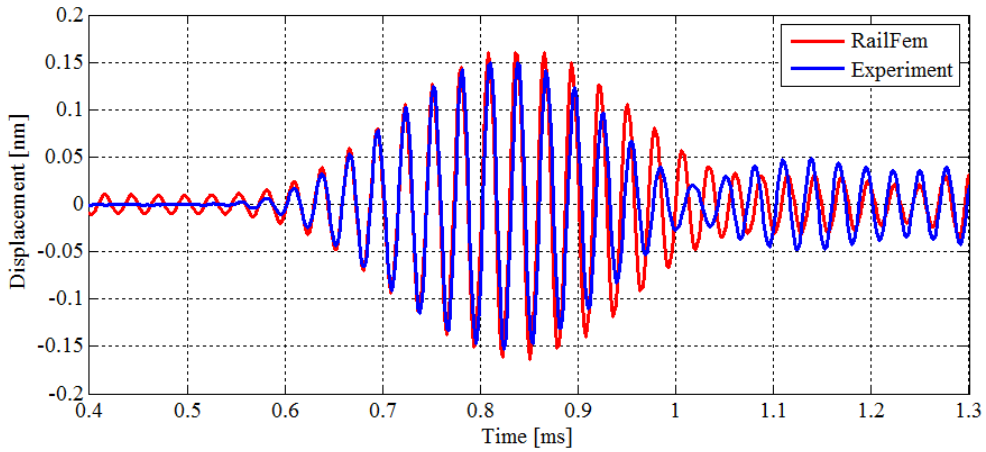

Figure 5.6: Response of the web mode when excited by an optimal transducer design.

The results demonstrate an exceptional agreement between SAFE-3D and the experiment.

5.4 Conclusion

Although the results from the resonance and anti-resonance frequency analyses in Section 5.2 are not trusted, the guided wave excitation results in Section 5.3 reveal that the manufactured transducer can be trusted since the correlation to SAFE-3D results is very good. The deviation of results in Section 5.2 calls for additional investigations regarding the factors affecting results.

CHAPTER 6

Conclusion and Recommendations

6.1 Conclusion

To upgrade the current version of the UBRD system, a piezoelectric transducer capable of exciting the rail web mode optimally is required. The web mode was identified as a forward propagating mode with energy concentrated in the web section of the rail. The mode is characterised by a flexural movement of the web section, with the head and the foot subjected to almost no displacement. At low frequencies of propagation, the web mode is highly dispersive. The mode becomes stable and less dispersive as the frequency gets higher. For $f \gtrsim 30kHz$, the dispersion of the mode is small. This characteristic makes the web mode a good candidate for defect detection since around this frequency and also at higher frequencies the velocity is almost constant indicating that the nature of the wave is subjected to almost a constant change with frequency.

The three objectives of this study were stated in Chapter 1. To conclude the study, each objective is stated again in this Section, followed by the associated outcomes.

Objective 1: To determine the strengths and weaknesses of the selected numerical modelling approach in predicting the response of waveguides to excitation.

Modelling of guided waves using the SAFE method is very efficient compared to other numerical modelling approaches. When correctly implemented, the method yields good results. However, under the assumption that the waveguide model is undamped, the method may yield unrealistic results due to cut-on frequencies. The effect of cut-on

frequencies can be avoided by adding damping to the model, filtering out frequency points associated with resonance behaviour, or by simply avoiding resonance frequencies by performing analyses at resonance-free frequency regions.

The main goal of this study was to design a piezoelectric transducer with an optimal performance at the operational frequency ($35kHz$) of the UBRD system. Since this operational frequency falls within a good frequency region of analysis, the cut-on frequency effects were avoided without having to implement any of the methods to counteract the problem.

Objective 2: To use the SAFE3D method and optimization techniques to design a piezoelectric transducer for exciting a mode with energy concentrated in the web of the rail.

A response surface-based optimization procedure with a Latin Hypercube sampled design of experiments was followed. A total of 500 sample designs were evaluated using the SAFE-3D method and then employed to construct the response surface of the objective function. The objective function values predicted by the response surface at selected designs outside the sample was found to be in good agreement with the function values when evaluated by the SAFE-3D method. A Nelder-Mead optimization algorithm was then used to find an optimal transducer design on the response surface, and the performance predicted by the response surface matched that computed from SAFE3D.

The good correlation between results indicate that the optimization procedure was successfully implemented and carried out. This outcome demonstrated the capability to automate the design of transducers for a particular rail cross-section and frequency range. The ability to collect 500 design samples using SAFE-3D proves that the method is computationally efficient and effective.

Objective 3: To manufacture the transducer and experimentally validate the modelling approach.

The web mode excitation results obtained from the SAFE-3D method were found to be in good agreement with experimental measurements. The validity of results reveals that for an undamped model, the method yields good results when the analysis is carried out at good frequencies.

The design method adopted in this study could therefore be used to automate the design of transducers for other sections of the rail or other frequencies of operation.

6.2 Recommendations

The following future work is recommended:

- Methods to counteract the unrealistic effects of cut-on frequencies should be investigated so that the SAFE-3D method can be used to design transducers for any frequency range.
- The results obtained from the transducer resonance and anti-resonance evaluations were found to be different between 3D FEM and the test measurement. Thorough investigations on the factors that resulted in this deviation need to be carried out.
- Field measurements of the optimal transducer need to be conducted to evaluate the performance of the transducer on a new rail with no cracks, and also on an old rail with cracks. It it important that the transducer allows for long range propagation of the web mode.

Bibliography

[1] E. V. Andhavarapu, P. W. Loveday, C. S. Long, and P. S. Heyns. Accuracy of Semi-Analytical Finite Elements for Modeling Wave Propagation in Rails. *Seventh South African Conference on Computational and Applied Mechanics*, (January), 2010.

[2] J. S. Arora. Chapter 1 - introduction to design optimization. In J. S. Arora, editor, *Introduction to Optimum Design (Third Edition)*, pages 1 – 15. Academic Press, Boston, third edition, 2012.

[3] J. S. Arora. Chapter 14 - practical applications of optimization. In J. S. Arora, editor, *Introduction to Optimum Design (Third Edition)*, pages 575 – 617. Academic Press, Boston, third edition, 2012.

[4] J. S. Arora. Chapter 2 - optimum design problem formulation. In J. S. Arora, editor, *Introduction to Optimum Design (Third Edition)*, pages 17 – 64. Academic Press, Boston, third edition, 2012.

[5] I. Bartoli, A. Marzani, F. Lanza di Scalea, and E. Viola. Modeling Wave Propagation in Damped Waveguides of Arbitrary Cross-section. *Journal of Sound and Vibration*, 295:685–707, 2006.

[6] F. A. Burger, P. W. Loveday, and C. S. Long. Large Scale Implementation of Guided Wave Based Broken Rail Monitoring. *41st Annual Review of Progress in Quantitative Nondestructive Evaluation*, (1650):771–776, 2015.

[7] R. D. Cook. *Finite Element Modeling for Stress Analysis*. John Wiley & Sons, Inc., 1995.

[8] V. Damljanovic and R. L. Weaver. Forced Response of a Cylindrical Waveguide with Simulation of the Wavenumber Extraction Problem. *The Journal of the Acoustical Society of America*, 115(4):1582–1591, April 2004.

[9] V. Damljanovic and R. L. Weaver. Propagating and Evanescent Elastic Waves in Cylindrical Waveguides of Arbitrary Cross Section. *The Journal of the Acoustical Society of America*, 115(4):1572–1581, April 2004.

[10] K. O. N. N. I. H. Elementov, S. Avdiaj, and N. Syla. MODELING OF THE PIEZOELECTRIC EFFECT USING THE FINITE-ELEMENT METHOD (FEM). 43(6), 2009.

[11] G. E. Fasshauer and J. G. Zhang. On Choosing "Optimal" Shape Parameters for RBF Approximation. *Numerical Algorithms*, 45(1–4):345–368, 2007.

[12] L. Gavric. Computation of Propagative Waves in Free Rail using a Finite Element Technique. *Journal of Sound and Vibration*, 185(3):531–543, 1995.

[13] T. Hayashi, W.-J. Song, and J. L. Rose. Guided wave dispersion curves for a bar with an arbitrary cross-section, a rod and rail example. *Ultrasonics*, 41(3):175–183, may 2003.

[14] T. Hayashi, W.-J. Song, and J. L. Rose. Guided wave dispersion curves for a bar with an arbitrary cross-section, a rod and rail example. *Ultrasonics*, 41(3):175–183, may 2003.

[15] H. Janssen. Monte-Carlo based uncertainty analysis: Sampling efficiency and sampling convergence. *Reliability Engineering and System Safety*, 109:123–132, 2013.

[16] J. Kim, B. L. Grisso, J. K. Kim, D. S. Ha, and D. J. Inman. Electrical Modeling of Piezoelectric Ceramics for Analysis and Evaluation of Sensory Systems. *SAS - IEEE Sensors Aplications Symposium*, pages 122–127, 2008.

[17] J. Kocbach, P. Lunde, M. Vestrheim, and J. Kocbach. Resonance Frequency Spectra with Convergence Tests of Piezoceramic Disks using the Finite Element Method. (47).

[18] W. Li, R. A. Dwight, and T. Zhang. On the Study of Vibration of a Supported Railway Rail using the Semi-analytical Finite Element Method. *Journal of Sound and Vibration*, 345:121–145, feb 2015.

[19] C. S. Long and P. W. Loveday. Prediction of Guided Wave Scattering by Defects in Rails Using Numerical Modelling. *40th Annual Review of Progress in Quantitative Nondestructive Evaluation*, 1581:240–247, 2014.

[20] P. W. Loveday. Simulation of Piezoelectric Excitation of Guided Waves using Waveguide Finite Elements. *IEEE Transactions on Ultrasonics, Ferroelectrics, and Frequency Control*, 55(9):2038–2045, 2008.

[21] P. W. Loveday and C. S. Long. Time Domain Simulation of Piezoelectric Excitation of Guided Waves in Rails using Waveguide Finite Elements. *Sensors and Smart Structures Technologies for Civil, Mechanical, and Aerospace Systems*, 6529:[6529–29], April 2007.

[22] P. W. Loveday and C. S. Long. Long Range Guided Wave Defect Monitoring in Rail Track. *40th Annual Review of Progress in Quantitative Nondestructive Evaluation*, 1581:179–185, 2014.

[23] A. Marzani. Time Transient Response for Ultrasonic Guided Waves Propagating in Damped Cylinders. *International Journal of Solids and Structures*, 45:6347–6368, December 2008.

[24] M. Mongillo. Choosing Basis Functions and Shape Parameters for Radial Basis Function Methods. *SIAM Undergraduate Research Online*, 4:190–209, 2011.

[25] M. W. Nygren. *Finite Element Modeling of Piezoelectric Ultrasonic Transducers*. PhD thesis, Norwegian University of Science and Technology, Department of Electronics and Telecommunications, 2011.

[26] V. Piefort. *Finite Element Modelling of Piezoelectric Active Structures*. PhD thesis, Universite Libre De Bruxelles, 2001.

[27] G. Qing, J. Qiu, and Y. Liu. A Semi-analytical Solution for Static and Dynamic Analysis of Plates with Piezoelectric Patches. *International Journal of Solids and Structures*, 43(6):1388–1403, 2006.

[28] S. Rippa. An Algorithm for Selecting a Good Value for the Parameter c in Radial Basis Function Interpolation. *Advances in Computational Mathematics*, 11:193–210, 1999.

[29] J. Rose. *Ultrasonic Waves in Solid Media*. Cambridge University Press, 2004.

[30] E. Saliby and F. Pacheco. An empirical evaluation of sampling methods in risk analysis simulation: quasi-Monte Carlo, descriptive sampling, and latin hypercube sampling. *Proceedings of the Winter Simulation Conference*, 2(Saliby 1990):1606–1610, 2002.

[31] H. Taweel, S. B. Dong, and M. Kazic. Wave Reflection from the Free End of a Cylinder with an Arbitrary Cross-section. *International Journal of Solids and Structures*, 37:1701–1726, 2000.

[32] F. Treyssède. Elastic Waves in Helical Waveguides. *Jorurnal of Wave Motion*, 45(4):457–470, March 2008.

[33] J. Yang. *An Introduction to the Theory of Piezoelectricity*. Advances in Mechanics and Mathematics. Springer US, 2004.

[34] J. Yin, W. Lu, X. Xin, and L. Zhang. Application of Monte Carlo sampling and Latin Hypercube sampling methods in pumping schedule design during establishing surrogate model. *ISWREP 2011 - Proceedings of 2011 International Symposium on Water Resource and Environmental Protection*, 1:212–215, 2011.

[35] O. Zienkiewicz, R. Taylor, and J. Zhu. *The Finite Element Method: Its Basis and Fundamentals*. Elsevier Science, 2005.

APPENDIX A

Element shape functions - SAFE method

The nodal displacement field is interpolated using Lagrange shape function, given by:

$$\begin{aligned} N_1 &= \frac{1}{4}(1-\xi)(1-\eta) \\ N_2 &= \frac{1}{4}(1+\xi)(1-\eta) \\ N_3 &= \frac{1}{4}(1+\xi)(1+\eta) \\ N_4 &= \frac{1}{4}(1-\xi)(1+\eta) \end{aligned} \tag{A.1}$$

The shape function interpolating matrix is constructed as:

$$\mathbf{N} = \begin{bmatrix} N_1 & 0 & 0 & N_2 & 0 & 0 & N_3 & 0 & 0 & N_4 & 0 & 0 \\ 0 & N_1 & 0 & 0 & N_2 & 0 & 0 & N_3 & 0 & 0 & N_4 & 0 \\ 0 & 0 & N_1 & 0 & 0 & N_2 & 0 & 0 & N_3 & 0 & 0 & N_4 \end{bmatrix} \tag{A.2}$$

The global coordinates of the element are expressed in terms of the natural coordinates ξ and η as:

$$x = \begin{Bmatrix} x \\ y \end{Bmatrix} = \sum_{i=1}^{4} N_i(\xi,\eta) \begin{Bmatrix} X_i \\ Y_i \end{Bmatrix} \tag{A.3}$$

In expanded form:

$$x = N_1X_1 + N_2X_2 + N_3X_3 + N_4X_4 \tag{A.4}$$

$$y = N_1Y_1 + N_2Y_2 + N_3Y_3 + N_4Y_4 \tag{A.5}$$

To perform coordinate transformation between the natural coordinates and the global coordinates, the Jacobian is used:

$$\mathbf{J} = \begin{bmatrix} \frac{\partial x}{\partial \xi} & \frac{\partial y}{\partial \xi} \\ \frac{\partial x}{\partial \eta} & \frac{\partial y}{\partial \eta} \end{bmatrix} = \begin{bmatrix} J_{11} & J_{12} \\ J_{21} & J_{22} \end{bmatrix} \tag{A.6}$$

The Jacobian contains information about the size of the element. The determinant of the Jacobian, is therefore used to relate the differential area of the element in the local coordinates to the differential area of the element in the global coordinates.

$$j = det(\mathbf{J}) = J_{11}J_{22} - J_{12}J_{21} \tag{A.7}$$

The inverse of the Jacobian is computed by:

$$\mathbf{J}^{-1} = \frac{1}{j} \begin{bmatrix} J_{22} & -J_{12} \\ -J_{12} & J_{11} \end{bmatrix} \tag{A.8}$$

The components of the Jacobian in equations A.6 to A.8 are given by:

$$\begin{aligned} J_{11} &= \frac{1}{4}\left(-\left(1-\eta\right)X_1 + \left(1-\eta\right)X_2 + \left(1+\eta\right)X_3 - \left(1+\eta\right)X_4\right) \\ J_{12} &= \frac{1}{4}\left(-\left(1-\eta\right)Y_1 + \left(1-\eta\right)Y_2 + \left(1+\eta\right)Y_3 - \left(1+\eta\right)Y_4\right) \\ J_{21} &= \frac{1}{4}\left(-\left(1-\xi\right)X_1 - \left(1+\xi\right)X_2 + \left(1+\xi\right)X_3 + \left(1-\xi\right)X_4\right) \\ J_{22} &= \frac{1}{4}\left(-\left(1-\xi\right)Y_1 - \left(1+\xi\right)Y_2 + \left(1+\xi\right)Y_3 + \left(1-\xi\right)Y_4\right) \end{aligned} \tag{A.9}$$

The shape function matrix is derived with respect to the global coordinates:

$$N_{,x} = \frac{\partial N}{\partial \xi}\frac{\partial \xi}{\partial x} + \frac{\partial N}{\partial \eta}\frac{\partial \eta}{\partial x} = \left[\frac{\partial x}{\partial \xi}\right]^{-1}\frac{\partial N}{\partial \xi} + \left[\frac{\partial x}{\partial \eta}\right]^{-1}\frac{\partial N}{\partial \eta} \tag{A.10}$$

$$N_{,y} = \frac{\partial N}{\partial \eta}\frac{\partial \eta}{\partial x} + \frac{\partial N}{\partial \xi}\frac{\partial \xi}{\partial y} = \left[\frac{\partial y}{\partial \eta}\right]^{-1}\frac{\partial N}{\partial \eta} + \left[\frac{\partial y}{\partial \xi}\right]^{-1}\frac{\partial N}{\partial \xi} \tag{A.11}$$

where

$$\frac{\partial N}{\partial \xi} = \begin{bmatrix} -(1-\eta) & 0 & 0 & (1-\eta) & 0 & 0 \\ 0 & -(1-\eta) & 0 & 0 & (1-\eta) & 0 \\ 0 & 0 & -(1-\eta) & 0 & 0 & (1-\eta) \\ (1+\eta) & 0 & 0 & -(1+\eta) & 0 & 0 \\ 0 & (1+\eta) & 0 & 0 & -(1+\eta) & 0 \\ 0 & 0 & (1+\eta) & 0 & 0 & -(1+\eta) \end{bmatrix} \quad \text{(A.12)}$$

$$\frac{\partial N}{\partial \eta} = \begin{bmatrix} -(1-\xi) & 0 & 0 & -(1+\xi) & 0 & 0 \\ 0 & -(1-\xi) & 0 & 0 & -(1+\xi) & 0 \\ 0 & 0 & -(1-\xi) & 0 & 0 & -(1+\xi) \\ (1+\xi) & 0 & 0 & -(1+\xi) & 0 & 0 \\ 0 & (1+\xi) & 0 & 0 & -(1+\xi) & 0 \\ 0 & 0 & (1+\xi) & 0 & 0 & -(1+\xi) \end{bmatrix} \quad \text{(A.13)}$$

Equations A.2, A.12 and A.13 can now be used to solve for the element matrices $\mathbf{B}_1$ and $\mathbf{B}_2$ as in equation 2.17 and 2.18 of Chapter 2.

APPENDIX B

Material properties

Young's Modulus, $[Gpa]$	210
Density, $[kg/m^3]$	7800
Poisson's ration	0.3

Table B.1: Material properties of UIC60 Rail

Dielectric constants, $[F/m]$	
ϵ_{11}^S	$2.298e-8$
ϵ_{22}^S	$2.298e-8$
ϵ_{33}^S	$3.532e-8$
Piezoelectric constants, $[c/m^2]$	
e_{31}	-2.918
e_{32}	-2.918
e_{33}	23.416
e_{24}	16.194
e_{15}	16.194
Stiffness, $[Gpa]$	
c_{11}^E	114.2
c_{12}^E	75.74
c_{13}^E	72.36
c_{33}^E	110.8
c_{44}^E	26.29
c_{55}^E	26.29
c_{66}^E	19.23
Density, $[kg/m^3]$	
ρ	7780

Table B.2: Material properties of Type IV piezoelectric ceramic

APPENDIX C

Computation of the transducer resonance and anti-resonance frequencies

The dynamic equations governing the piezoelectric behaviour are given by:

$$[M_{uu}]\{\ddot{u}\} + [K_{uu}]\{\dot{u}\} + [K_{u\phi}]\{\phi\} = [f] \tag{C.1}$$

$$[K_{u\phi}]^T\{u\} + [K_{\phi\phi}]\{\phi\} = -\{q\} \tag{C.2}$$

where M_{uu} is the mass matrix, $[K_{uu}]$ is the mechanical stiffness matrix, $[K_{u\phi}]$ is the piezoelectric stiffness matrix and $[K_{\phi\phi}]$ is the dielectric stiffness matrix. The mechanical force and displacement are respectively defined by $\{f\}$ and $\{u\}$, while the electrical charge and potential are respectively defined by $\{q\}$ and $\{\phi\}$.

The system in C.1 and C.2 can be written in H-form as [17]:

$$[M_{uu}]\{\ddot{u}\} + [H_{uu}]\{\dot{u}\} + \{H_{u\phi}\}\phi = [f] \tag{C.3}$$

$$\{H_{u\phi}\}^T\{u\} + \{H_{\phi\phi}\}\phi = -q_p \tag{C.4}$$

where

$$\tag{C.5}$$

$$[H_{uu}] \;=\; [K_{uu}] - [K_{u\phi_i}][K_{\phi_i\phi_i}]^{-1}[K_{u\phi_i}]^T, \tag{C.6}$$

$$\{H_{u\phi}\} = \left(\left[K_{u\phi_p}\right] - \left[K_{u\phi_i}\right]\left[K_{\phi_i\phi_i}\right]^{-1}\left[K_{\phi_i\phi_p}\right]\right)[I_p]\,, \tag{C.7}$$

$$H_{\phi\phi} = [I_p]^T\left(\left[K_{\phi_p\phi_p}\right] - \left[K_{\phi_i\phi_p}\right]^T\left[K_{\phi_i\phi_i}\right]^{-1}\left[K_{\phi_i\phi_p}\right]\right)[I_p]\,. \tag{C.8}$$

In equations C.6 to C.8 the degrees of freedom on the piezoelectric material are partitioned into those on the non-grounded electrode (p) and those which are on the internal (i) and not on any of the electrodes. $[I_p]^T = \begin{bmatrix} 1 & 1 & 1 & \dots & 1 \end{bmatrix}$ is a vector with length equal to the number of degrees of freedom on the electrode with varying potential, and q_p is the charge induced on that electrode.

Assuming a harmonic time dependence, the resonance frequencies are found by setting the mechanical force as well as the electric potential on the grounded and non-grounded electrodes to zero. The eigenvalue problem for resonance frequencies is thus defined by:

$$\left([H_{uu}] - \omega_r^2\,[M_{uu}]\right)\{\psi_r\} = 0 \tag{C.9}$$

where $\{\psi_r\}$are the eigenvectors corresponding to the resonance frequencies ω_r.

To compute the anti-resonance frequencies, the we only set the mechanical force and the electrical potential on the grounded electrode to zero. The resulting eigenvalue problem is:

$$\left\{[H_{uu}] - \{H_{u\phi}\}\,H_{\phi\phi}^{-1}\,\{H_{u\phi}\}^T - \omega_a^2\,[M_{uu}]\right\}\{\psi_a\} = 0 \tag{C.10}$$

where $\{\psi_a\}$are the eigenvectors corresponding to the anti-resonance frequencies ω_a.